

Fluid-Structure Interaction (FSI) case study of a
cantilever using OpenFOAM and DEAL.II with
application to VIV

Johan Lorentzon

June 17, 2009

Thesis for the degree of Master Science in Technical Mathematics.
ISSN 0282-1990
ISRN LUTMDN/TMHP-09/5186-SE

©Johan Lorentzon, Juni 2009
Division of Fluid Mechanics
Department of Energy Sciences
Lunds Institute of Technology
Box 118
S-211 00 LUND
Sweden

Abstract

This Master Thesis in Technical Mathematics at LTH, directed towards simulation and computation, has treated the subject of fluid-structure interaction (FSI) for incompressible flow with small vibrations. The open source packages DEAL.II and OpenFOAM have been used to create a coupling between a finite element formulation for structure and a finite volume formulation for fluid (gas or liquid). A staggered solution algorithm for FSI has been implemented in C++ using Aitkens relaxation method together with a Reduced-Order-Model (ROM). The solution algorithm has been validated by using an application consisting of a cantilever immersed in a steady flow transversal to its axial direction. Also, vortex-induced vibrations (VIV) were calculated as a function of the flow velocity and successfully compared to empirical data. The study has demonstrated the usefulness of artificial damping to solve boundary condition problems in incompressible flow. The method presented is general and has a strong potential in technical applications where the structure is subjected to a surrounding fluid.

Acknowledgement

To my supervisors, Johan Revstedt, Robert Zoltan Szasz, Per Erik Austrell: My thanks for being supportive in my work. To my friend Mathias Haage, I am truly grateful for your encouragement as consultant in the field of C++. The teachers Per Lidström, Matti Ristinmaa, Mathias Wallin, Claus Führer, Niels Saabye Ottosen and Jan Gustavsson my thanks for enduring my endless questions in the field of continuum mechanics and mathematics. I would also like to thank Gunnar Sparr, for the gift of the precious compendium "Kontinuerliga system" from year 1983, the very same version i lost on the train last year, a compendium that truly inspired me in my work. Finally, my thanks to my mentor Andrej Sadlev, for the years of fruitful discussions and meetings in the topic applied mathematics.

December 2008.

Nomenclature

Abbreviations

BC	Boundary Condition
CFD	Computational Fluid Dynamics
Co	Courant number
cv	control volume
FD	Finite Difference
FEM	Finite Element Method
FIV	Flow-Induced Vibrations
FSI	Fluid-Structure Interaction
FVM	Finite Volume Method
INS	Incompressible Navier Stokes Equation
KC	Keulegan Carpenter Number
PDE	Partial Differential Equation
Re	Reynolds number
ROM	Reduced Order Model
St	Strouahls number
VIV	Vortex-Induced Vibration

Mathematical notation

Tensor notation is adopted to distinguish tensor A_i from vector notation \mathbf{A} , and this implies the convention [12] of summation index,

$$A_i B_i = \sum_k A_k B_k, \quad (1)$$

and the differential convention for tensor,

$$A_{j,i,i} = \sum_k \partial_k A_{jk}. \quad (2)$$

The difference between vector and tensor is the applied rule upon coordinate transformation for a tensor. Although, ambiguity in interpretation of formulas appears, a vector in this thesis is a representation of a tensor. The origin of these rules comes from the that since physical laws are invariant to coordinate transformations and when expressed in tensor notation the physical constants also shall be invariant.

Symbols

A	m	Amplitude of marker point
A_t	m^2	Area of the tip of cantilever
b	Nm^{-3}	Force per volume
C	$kg s^{-1}$	Damping matrix
D	m	Width of cantilever
E	Pa	Young's Modulus
f	s^{-1}	VIV frequency
f^S	N	Force acting on structure
f^F	N	Force acting on fluid
f_n	s^{-1}	Natural frequency of structure
I	m^4	Moment of inertia
K	Nm^{-1}	Stiffness matrix
L	m	Height of cantilever
l	m	Characteristic length
M	kg	Mass matrix
n		Surface normal
p	Pa	Pressure
ΔP	Pa	Pressure difference
q	m	Displacement field of structure
t	Pa	Traction vector
T_r	s	Reference time period
T_c	s	Calculated time period
T_v	s	Vacuum time period
U	ms^{-1}	Flow velocity
U	ms^{-1}	Magnitude of velocity at inlet
U_r	ms^{-1}	Relative velocity
v	ms^{-1}	Velocity field of structure
V_r	ms^{-1}	Reduced velocity
ϵ		Symmetric gradient operator
μ^*	$m^2 s^{-1}$	Kinematic viscosity
μ	$kg m^{-1} s^{-1}$	Viscosity
ρ_f	$kg m^{-3}$	Density of flow
ρ_s	$kg m^{-3}$	Density of structure
ω	s^{-1}	Forced frequency
ν		Poisson number
σ	Pa	Stress

Contents

1	Introduction	3
1.1	The Scenario	3
1.2	Background	4
1.3	Outline of the FSI algorithm	5
1.4	The motivation	6
1.5	Objective of the thesis	8
1.6	The material used for this thesis	8
2	Theory	9
2.1	The Continuum hypothesis	9
2.2	Numerical approach	9
2.3	Governing equations for the incompressible flow	10
2.4	The Finite Volume Method applied to the INS	11
2.5	Quasi-steady approximation	13
2.6	Weak form for static system of the solid state	14
2.7	The Finite Element Method	15
2.8	Governing equation in the state space formalism	15
2.9	ALE description and imposed BC	17
2.10	The Fluid-Structure Interaction	17
2.10.1	Monolithic FSI Problem	17
2.10.2	Staggered FSI algorithm	18
2.11	Acceleration of the convergence	19
2.11.1	Aitkens relaxation method	19
2.11.2	The ROM method	19
3	Implementation	21
3.1	The compilation	21
3.2	Main program ICOFSI	21
3.3	OpenFOAM Package	23
3.4	DEAL.II package	24
3.5	InterGridMapping	26
3.5.1	Mapping functions	26
3.5.2	Transfer step	26
4	The case study	27
4.1	Beam theory of the cantilever	27
4.2	The steady state response for a cantilever.	27
4.3	Boundary condition	28

4.4	Single cantilever study	29
4.5	Multi-block cantilever study	30
4.6	The cantilever mesh	31
4.7	The fluid domain mesh	32
5	Validation procedure	33
5.1	Solid state solver	33
5.1.1	Test Case	33
5.1.2	Verification of class StaticElastic	34
5.1.3	Verification of class QuasiElasticity	34
5.1.4	Verification of the class DynamicElastic	35
5.2	icoDyMFoam	37
5.3	setBoundaryIndicator and InterGridMapping	37
5.4	The FSI algorithm	38
5.4.1	Setup	38
5.4.2	A note on measurement of the period	38
5.4.3	Result	39
5.5	Error analysis	47
5.5.1	icoDyMFoam	47
5.5.2	DynamicElastic	47
5.5.3	Estimated Error in the period	48
5.6	General comments	52
5.6.1	The theta method	52
5.6.2	Explicit/Implicit FSI	52
5.6.3	Aitkens relaxation and the ROM	53
5.7	Multiple block case	54
5.8	Conclusion	55
6	An application to VIV	57
6.1	Problem description	57
6.2	Setup	57
6.3	Result	58
7	Discussion	67
8	Future work	71

Chapter 1

Introduction

This chapter describes the scenario and the incentive for this study. The background of fluid-structure interaction and its technical applications is presented with a brief description of the vortex-induced vibration. This is followed by an outline of the staggered algorithm and ends with a survey of the research field on this subject which defines the goals of the thesis and the material used.

1.1 The Scenario

A cantilever is placed in a domain of a velocity driven fluid. The stress acting upon the structure induces a deformation of the structure to which the fluid responds. This mutual influence referred to as fluid-structure interaction (FSI), is known to cause several interesting phenomena. Among such is vortex-induced vibration, where the forced movement of a fluid around the structure gives upon point of release from the structure, an angular momentum manifested as a vortex in the fluid. Further, due to no-slip condition between fluid and structure, the structure will experience an extra mass while moving and hence decrease the natural frequency.

For this simple case there is an analytical formula for the steady FSI but already when including the effect of confining walls the task becomes quickly overwhelming while using pencil and paper. At this point the computer is unhanding us this problem. This requires a theory to model the FSI and a numerical procedure such that when the problem is implemented, a computer simulation can give us an approximate answer to our problem. Although every step is simple from a mathematical point of view, the number of steps can be an exerting task for even a skilled scientist. An efficient engineer takes the work of others and reshapes their tools for his own purpose.

The computer can be instructed in several languages, each language fulfilling their purpose. For many years *Fortran* has been considered as the key language for a computational engineer due to its efficient implemented libraries and compilers adapted to high-speed machines different from PC. However, as the architecture of the computer changes the difference becomes more vague and favor Object-Oriented (OO) languages such as *C++/Java/Python* which minimizes the development time and spread the usability to far more users due to its simplicity in implementation [70, 74]. Without further dwelling into details, the actual question that matters is how to organize the work and how fast it can be implemented, not how much faster the code will become or easier it is to code on a detailed level.

1.2 Background

The Fluid-Structure Interaction (FSI) appears as a physical phenomenon in engineering [13] such as static load, drag, and Flow-Induced-Vibrations (FIV). FIV is further classified into flutter, galloping and vortex-induced vibrations (VIV) [32]. The static load on the structure originates mainly from the total pressure difference between front and wake side of the structure. The dynamic pressure can due to instability in the structure, where the damping is less than the energy transferred by the vortex-induced wake, create a resonance with the structure with a negative damping known as flutter.

Alternatively it will be manifested as VIV, where the pressure difference created by the vortices causes an elastic response in the structure with smaller amplitudes inducing fatigue cycles on the structure. A related issue is buffeting, which mainly concern the turbulence random excitation on the structure. Galloping falls between the regime of flutter and VIV. The classification of FIV is however not precise where overlaps between the areas are a common thread to misunderstanding. However, the VIV gives the answers to a large number of questions involved in this phenomenon of FSI,

- Estimation of the structural response to a given flow.
- The mechanism behind the coupling between fluid and structure.
- Estimation of the fatigue in structure.
- Design structure to minimize the self-induced vibrations.

The questions are related to each other but focused on different aspects: prediction, understanding and prevention. Typical examples of applications in which flutter is considered are aircraft wings, tall buildings, rotating blades and long-span bridges [51, 47, 48]. The VIV concerns bridges [59], chimneys [10], heat exchanger tubes [45], power lines and undersea constructions such as sea cables/risers [18, 9] or biomechanical applications as blood vessels [53].

A simplified case of self-induced vibration is forced vibrational study where the oscillation to given frequency ω of the structure in transversal direction to given flow direction creates a coupling force with the surrounding fluid. Several studies have showed a lock-in frequency with the fluid's frequency of vortex shedding, f . In a review by Williamson [58], focused on cylinder/cantilever, experiments and models explains the phenomenon thoroughly. In this review, the reduced velocity V_r ($\frac{U}{\omega l}$) versus $\frac{f}{\omega}$ show a linear dependency except for a region around $\omega = f$. The cylinder/cantilever or fin motion behind bluff body in enclosed compartments are classical applications allowing self-induced vibrations [20, 38, 31]. Further, V_r versus the reduced amplitude in transversal direction to the flow for self-induced free vibration $\frac{A}{l}$ show a coupling between the form in release of vortex and the magnitude of reduced amplitude response. The results implicate that a steady state motion turns into a unsteady motion for a certain frequency ω irrelevant to the size of the body. At this point it is evident of the importance in understanding the synchronization of a wake mechanism with the movement of the structure.

From this knowledge a passive control [6, 32, 10] of FIV can be developed to prevent damaging effects of short term [24] and long term [45] effects on the structure. However, the characteristic of the vortex shedding depend on the structure [31, 26, 24]. The simplest mode of vortex shedding is the one studied in the cylinder case, where the alternate release of vortex is observed as a street of pairs of vortices with opposite spin, denoted as 2S mode. This is a direct consequence when taking the bluff body effect into consideration. This effect

forces the fluid to take a curved path which at point of release have a curl with same the spin as the flow around the body, a Vortex is born, see Figure 1.1. The next type of mode is 2P appearing when the lock-in frequency cause a phase shift in which the FSI coupling creates two pair of vortices within each periodic cycle hence four vortices per cycle. The design to

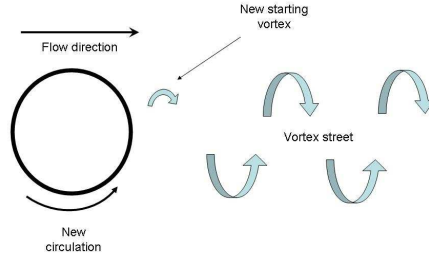


Figure 1.1: A principal sketch of a 2S vortex formation process [42].

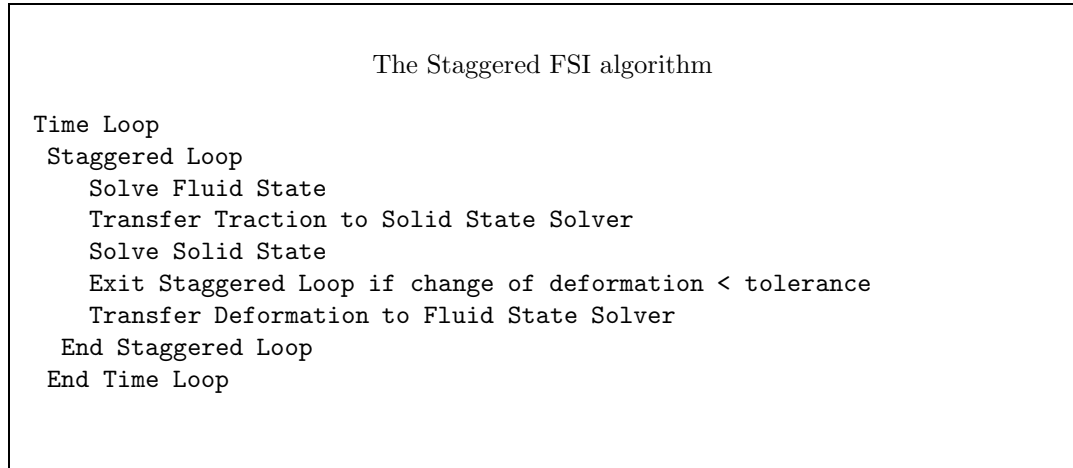
prevent these phenomena is however not always the same and to analyze a problem as an engineer requires skills in empirical estimating the factors of influence. An infamous example of such failure in estimating the effect of dynamics of the flow is the Tacoma bridge which also illustrates the misconception between cause and consequence. The flutter is the cause to the collapse and there was no lock-in between VIV and the natural frequency of the structure [7, 24]. Still, the pre-loading of the structure could have its source from VIV.

Although the question of difference seem semantic, since both phenomena are self-induced vibrations, it is noted that this is an event that has been debated over a half century. In the process to develop a passive control of VIV, a Direct Numerical Simulation to support experimental investigation is desirable. This minimize the cost involved with reinforcement and maintenance.

1.3 Outline of the FSI algorithm

Fluid mechanics is characterized to be a highly chaotic dynamical system and solid mechanics by its self preserving and elastic behavior. The governing equations expressed in PDE and their characteristics could therefore be different, changing from hyperbolic/parabolic to elliptic. By implementing the whole fluid-structure interaction in one solver, also known as the monolith approach [25, 8], requires more computational effort and may lead to less accurate simulation due to the limitation in the modeling. This loss in accuracy has its origin mainly in that the numerical method depends on the characteristic of PDE where a system that changes characteristic during simulation requiring projection techniques solved by introducing intermediate variables which split the moment equation into sub-equations or by using semi-discretization techniques and assume flow characteristic such as incompressible flow. In both cases stability criteria arises and error is introduced, although in different senses, numerical and modeling error respectively. The second aspect in loss of accuracy is the limitation of the computational resources, which requires a cut-off in precision. However, the traditional way to solve equations of this type is by using the staggered technique [37, 33]. The staggered solver exchanges the interaction term in an iterative scheme by solving each domain separately. The particular advantage of this method is the possibility to use a black box solver for each governing equation, and with a small effort merge them into a functional

FSI algorithm. This implicates the possibility to use different solution techniques that enables a more accurate modeling.



The accuracy is thus affected by restricting the governing equation in PDE form to a given characteristic, or refine the constitutive modeling and/or using the staggered techniques which formulates the linear matrix equations as symmetric, while the monolith approach leads to asymmetric ones. The problematic part is that the staggered technique for the incompressible case suffer severely by stability issues. This occurs whenever the change in variables under each iteration induce a change such that when inserted into the equation, the residual is of comparable size as the coupling term. Improper BC conditions also affect this due to the domain of dependency for incompressible flow.

1.4 The motivation

ANSYS+CFX [64] have both monolith and staggered techniques available, ABAQUS and FLUENT [63] have been used in several studies, COMSOLE MULTIPHYSICS [62] has a module for both techniques. The commercial products give low insight in solution techniques and their verification is built upon cases which can be downloaded and tested against other codes using open source, but any manipulation of the algorithm itself is limited although some has console window option allowing meta-coding. The usage of the staggered technique with ABAQUS and FLUENT gives elaborate choice of tool box and solution techniques for each domain separately. However, the COMSOLE MULTIPHYSIC gives the full control of the solution techniques but compared to ANSYS+CFX 11.0 it is less efficient to a factor of three using the version 3.4 [62, 66]. Other commercial products of interest are ADINA [4] and LS-DYNA [67].

For university applications, it is however important apart from the license cost benefit, both from an educational and a research point of view to be able to modify the algorithm. There are several open source codes for solving FSI. The solvers implemented by individual research teams often fall within the categories of staggered, monolith or approximative modeling. Further, one can distinguish between stochastic approach and deterministic.

One solver of interest is the *icofsi* solver from OpenFOAM developed by Tukovic and Jasak [53]. This is a solver based on the Finite Volume Method (FVM) using Green-Cauchy strain measure that allow arbitrary deformations with application to a cantilever in a rectangular

domain. This article use the Aitkens under-relaxation technique to accelerate the convergence of the fully coupled FSI is presented and the difference is demonstrated between explicit and implicit FSI. The monolith method suffer from the ill-conditioned system matrix and precision loss due to computational limitation, but there is an approach to solve this [25] by using a fluid Pressure Poisson Equation for INS. The validation of this algorithm is based upon calculating the added mass and study VIV on a cylinder immersed in a velocity driven domain.

To improve the convergence of the monolithic approach, an article by M. Razzaq *et al* presented a Newton-Raphson scheme using a Finite-Difference scheme (FD) to evaluate the Jacobian [43] and a similar approach is performed with a staggered method [37]. A step further is the reduced-order model (ROM), where the governing equations are replaced by a local estimate of the PDE by using a FD scheme or a residual method. This is used either as a preconditioner in the sub-cycle or replaces the solver to save computational effort [54, 16]. In the staggered solution technique, allowing parallel execution is an essential step in order to maintain a simulation within a reasonable time and to a limited cost solve larger structures. Several articles have been presented on this subject but [15] highlights the instability region where one falsely concludes the flutter point due to the explicit staggered scheme. This article also further points out the limitation in fully coupled in precision due to small time step required and emphasis the need of adaptive time stepping to achieve convergence. In the effort to stabilize the fully coupled staggered algorithm the Aitkens Δ^2 relaxation method was implemented with successful result [33, 53].

A topic not included in this thesis is the turbulence, which add the buffeting effect in FSI, this is vital since the random excitations on a structure have a significant effect on durability and in aeroelasticity [50]. In all discussed articles above use the Arbitrary Lagrangian-Euler description essential for FSI and for an excellent review by J.Donea *et al* on the topic see [11]. The list of individual contributions in FSI is vast, for further see review by Dowell [13] and references therein or the Wikipedia link [72].

1.5 Objective of the thesis

This thesis has the goal to implement an implicit FSI algorithm by coupling a CFD and a FEM solver. Then validate the FSI solver by reproducing the common phenomena observed such as VIV and frequency/amplitude shifts, then analyze and optimizing its performance. The code should have generic input allowing different types of mesh to be used. Another goal is to generalize the algorithm to multiple structures that enable differentiation in modeling. The code is restricted to elastic modeling with small strain of the structure with limited adaptive meshing. The programming language is C++ with the goal to create an interface such that it can easily be developed to include non-linear basis elements, non-linear strain, under-integrations techniques, accelerated techniques in convergence and adaptive meshing in each time step. The effort is merely replace/adding a class in the code.

1.6 The material used for this thesis

The open source packages used in this project are OpenFOAM [27, 65] and DEAL.II[61]. This allows to run the FSI solver on separate machines/threads. The original application is taken from an article by Sampaoi [50] but using the staggered algorithm and parameter settings presented by Tukovic and Jasak [53]. An article by M. Dreier *et al* [55] about the natural frequency shift of a cantilever immersed in a fluid is used in order to verify the solver since suitable experimental data for the given case and free vibrational study were not be found. In order to increase the performance, the reduced-order model (ROM) was implemented using the article by Vierendeels as guidance [54]. Further, to accelerate/stabilize the sub-cycle loop in the staggered technique, and to locate the quasi-static equilibrium point between the solvers by the fix-point iteration, the Aitkens relaxation method was chosen. This method is described by Küttler and Wall [33]. An important resource is the forum sites associated with the homepages for each open source package. The developers and several research teams report their issue and share knowledge and experience which is very valuable for a beginner on the subject.

Chapter 2

Theory

The problem can be divided into three domains. First, the physical domain, the container of our phenomena of interest, formulated in terms of physical laws and variables. Secondly, the model domain, the set of approximations describing the physical domain to be governed by equations in PDE. Finally, the numerical domain containing the procedure in how to implement and solve the PDE in a computer environment. This chapter first discusses the limits of the control volume size where constitutive relation is relevant, then distinguish the difference between FVM and FEM. The governing equations describing each domain is derived and the boundary conditions and explicit formulas used in this thesis will be discussed.

2.1 The Continuum hypothesis

The concept used in this thesis is the deterministic behavior of physical domain allowing functional relation between variables. This is when the molecular fluctuations becomes infinitesimal and statistical mechanics enters the realm of continuum mechanics. The essential part is the macroscopic model description where constitutive equations interrelate to the variable representing the physical quantities of interest. The model description of a physical domain is often expressed in terms of governing equations, a set of state equations whose state variables are related by PDE in strong form or as state functions. The validity of the continuum hypothesis can often be estimated by evaluating the size of a given control volume δV when the statistical fluctuations of a given parameter becomes negligible. Although this limit is a gray-scale, less than $1 \cdot 10^{-6}m$ in cell diameter, the statistical description becomes significant, and at $1 \cdot 10^{-9}m$ quantum effects cannot be neglected.

2.2 Numerical approach

Given the model expressed in PDE, the problem can be solved in two fundamentally different ways, either one discretize the operators and then solves the parameter relation, or one discretizes the solution space and uses the exact PDE to define a residual which is to be minimized. The different approaches can then of course be combined. The mesh is the topology together with the grid that defines the solution space to a given problem. Discretize the PDE consistently with ensured stability, then in the limit of infinitesimal mesh the Finite Difference scheme (FD) will approach the exact solution. Another approach is to integrate the strong form over the control volume, and even further partial integrate into a weak form

of the system, where a solution to a strong PDE is the solution to a weak form but not necessary the other way around. It is under this category the Finite Volume Method (FVM) enters using a conservative form of the PDE. The other approach is to multiply the strong form with a test function, then from this its weak form is formulated. This leads to a bilinear form which defines a linear system, whose solution in the limit of infinitesimal mesh goes to the exact solution of the original strong PDE form. A general applied method is the Galerkin method where the test functions are chosen to be the discretized solution space, the FEM method.

2.3 Governing equations for the incompressible flow

The continuity equation states that for a given property ϕ for a given infinitesimal volume element δV with the flux \mathbf{F} , the sum of the unsteady change of the ϕ and the change in flux is equal to the source S_ϕ ,

$$\partial_t \phi + \nabla \cdot \mathbf{F} = S_\phi. \quad (2.1)$$

By applying the conservation of mass $S_\phi = 0$, setting $\phi = \rho_f$ and $\mathbf{F} = \phi \mathbf{U}$, where \mathbf{U} is the velocity through given δV of the fluid, then the continuity equation for mass becomes

$$\partial_t \rho_f + \nabla \cdot (\rho_f \mathbf{U}) = 0. \quad (2.2)$$

Define the material time derivative as

$$\frac{D}{Dt} = \partial_t + \mathbf{U} \cdot \nabla. \quad (2.3)$$

By identifying the material time derivative in Eqn (2.2) the expression takes the following form

$$\frac{D\rho_f}{Dt} = -\rho_f(\nabla \cdot \mathbf{U}). \quad (2.4)$$

Incompressible flow is characterized by a zero material derivative which implies the condition

$$\nabla \cdot \mathbf{U} = 0. \quad (2.5)$$

Applying the conservation of momentum to the Eqn (2.1), defining $\phi = \rho_f U_i$ and the flux $\mathbf{F} = \phi \mathbf{U}$, using the conservation of mass, the Newton's second law can be identified with LHS and therefore the source term becomes the force f_i ,

$$\rho_f \frac{DU_i}{Dt} = S_\phi \equiv f_i. \quad (2.6)$$

Using continuum mechanics on f_i , defining b_i as the body force acting per volume, and stress tensor σ_{ij} acting upon the boundary, the equation of motion is given by,

$$f_i = \sigma_{ij,j} + b_i. \quad (2.7)$$

At this point, this applies to both fluid and solid mechanics and the equation formed by Eqn (2.6) and Eqn (2.7) is a part of the Incompressible Navier Stokes equations (INS). The difference lies upon the constitutive relation defined for the shear stress part of the stress tensor, τ_{ij} ,

$$\sigma_{ij} = -p\delta_{ij} + \tau_{ij}. \quad (2.8)$$

For a Newtonian fluid using symmetric gradient $\epsilon = \frac{1}{2}(\nabla + \nabla^T)$,

$$\tau_{ij} = \lambda(\nabla \cdot \mathbf{U})\delta_{ij} + \mu(\partial_j U_i + \partial_i U_j) = \lambda(\nabla \cdot \mathbf{U})\delta_{ij} + 2\mu\epsilon_{ij}(\mathbf{U}), \quad (2.9)$$

where $\lambda \geq -\frac{2}{3}\mu$ in order to satisfy entropy condition [52], where the Stokes condition assert equality. Using the incompressibility condition Eqn (2.5) on Eqn (2.9), then Eqn (2.6) becomes ($\nabla^2 = \nabla \cdot \nabla$)

$$\rho_f \frac{D\mathbf{U}}{Dt} = -\nabla p + \mu \nabla^2 \mathbf{U} + \mathbf{b}. \quad (2.10)$$

The conservation of angular momentum has to be taken into consideration, this gives the condition of symmetric stress tensor ($\sigma_{ij} = \sigma_{ji}$) as Eqn (2.9) provides. Denote l as the characteristic length, a the reference speed, define then $\mathbf{U}^* = \frac{\mathbf{U}}{a}$, $t^* = \frac{ta}{l}$, $x_i^* = \frac{x_i}{l}$, $p^* = \frac{p}{\rho_f a^2}$, $\mu^* = \frac{\mu}{\rho_f}$ and $\nabla^* = l\nabla$, the following dimensionless governing equation is obtained,

$$\nabla^* \cdot \mathbf{U}^* = 0, \quad (2.11)$$

$$\frac{D\mathbf{U}^*}{Dt^*} = -\nabla^* p^* + \frac{1}{Re} \nabla^{*2} \mathbf{U}^* + \mathbf{b}^*, \quad (2.12)$$

where $Re = \frac{al}{\mu^*}$ is the Reynolds number. Note, OpenFOAM CFD package have not adopted the convention to scale velocity, only the pressure. The equations originating from the energy conservation is omitted in this thesis.

2.4 The Finite Volume Method applied to the INS

The center value Finite Volume Method (FVM) uses the conservative integral forms of the governing equations of the fluid characterized by the following [17, 28],

- spatial derivatives over volume are converted into integrals over surfaces in terms of the flux \mathbf{F} .
- time derivative is semi-discretized.
- the grid points define the faces and the discretization reservoir points are at the center of the control volume (cv).
- the fluxes are interpolated at each step.
- the integrals are evaluated by the use of the mean value theorem.

In applying the FVM for INS, the strong form of the PDE for the INS is integrated over a control volume (cv). This control volume is polyhedral, arbitrary as long it is convex and has planar surface elements. The physical reservoir point P is at the centroid \mathbf{x}_P of the cv, the interior domain/volume V_P . Each given face k of the cv has its centroid point \mathbf{x}_k and the neighbor N.

By Taylor expansion of the tensor to the first order around the centroid of the cv, the integration error becomes to the second order accurate with the size of the cv,

$$\phi = \phi_P + (\mathbf{x} - \mathbf{x}_P) \cdot \nabla \phi(\mathbf{x}_P) + O(\|\mathbf{x}\|^2). \quad (2.13)$$

The face values ϕ_k of the ϕ of the \mathbf{x}_P is estimated by the Central Difference (CD) approximation,

$$(\phi)_k \approx \frac{\|\mathbf{x}_k - \mathbf{x}_P\|}{\|\mathbf{x}_P - \mathbf{x}_N\|} \phi(\mathbf{x}_P) + \left(1 - \frac{\|\mathbf{x}_k - \mathbf{x}_N\|}{\|\mathbf{x}_P - \mathbf{x}_N\|}\right) \phi(\mathbf{x}_N). \quad (2.14)$$

and defining $\mathbf{S}(\mathbf{k})$ to be the face surface normal with the magnitude of the area of the face k , then $\mathbf{S} \cdot (\nabla\phi)_k$ is approximated by,

$$\mathbf{S} \cdot (\nabla\phi)_k \approx \|\mathbf{S}\| \frac{\phi_N - \phi_P}{\|\mathbf{x}_N - \mathbf{x}_P\|}. \quad (2.15)$$

However, CD cause unbounded solutions whenever convective term is the dominating term [28]. In non-orthogonal meshes, a correction term appears that is omitted here for simplicity for all flux and face values. In similar fashion for second order temporal discretization the error is proportional to $(\Delta t)^2$.

The INS (2.5) and (2.6) become with $\phi_i = \rho_f U_i$ and definitions from previous section,

$$\int_{V_P} \nabla \cdot \mathbf{U} dV = 0, \quad (2.16)$$

$$\int_t^{t+\Delta t} \left[\frac{\partial}{\partial t} \int_{V_P} \phi_i dV + \int_{V_P} \nabla \cdot (\phi_i \mathbf{U}) dV + \int_{V_P} \partial_i p dV - \mu \int_{V_P} \nabla^2 \phi_i dV \right] dt = 0. \quad (2.17)$$

Define the $F(k) = \mathbf{S} \cdot (\phi)_k$ as the numerical mass flux. Using the divergence theorem on the convective term, taking ϕ_i to be the value in cv P at \mathbf{x}_P this term then becomes

$$\int_{V_P} \nabla \cdot (\mathbf{U} \phi_i) dV = \int_{\partial V_P} \mathbf{U} \phi_i \cdot \mathbf{dS} \approx \sum_k F(U_i)_k. \quad (2.18)$$

Taking the transient part of Eqn (2.17) to be semi-discretized by using implicit Euler scheme where superscript n is an index to time t_n . Use Eqn (2.18) to discretize the convective term, and by using divergence theorem on the diffusion term together with Eqn (2.15), then the LHS of Eqn (2.17) becomes

$$\int_t^{t+\Delta t} \left[\left(\frac{(\phi_i^n)_P - (\phi_i^{n-1})_P}{\Delta t} \right) V_P + \sum_k S_i(p)_k + \sum_k F(U_i^n)_k - \sum_k \mu \mathbf{S} \cdot (\nabla \phi_i^n)_k \right] dt. \quad (2.19)$$

By assuming no change in the control volume V_P , the update scheme then becomes,

$$(\phi_i^n)_P = (\phi_i^{n-1})_P + \frac{\Delta t}{V_P} \left[\sum_k S_i(p)_k + \sum_k F(U_i^n)_k - \sum_k \mu \mathbf{S} \cdot (\nabla \phi_i^n)_k \right]. \quad (2.20)$$

By this scheme in Eqn (2.20), a stability condition is introduced, the so called Courant number $Co = \left| \frac{\mathbf{U}_f \cdot (\mathbf{x}_P - \mathbf{x}_N)}{\Delta t} \right| < 1$. In the implicit Euler scheme the flux and gradient of the flux is calculated on the current time scale n in accordance to Eqn (2.14) and Eqn (2.15). The INS is non-linear in the convective term. For each cv Eqn (2.20) defines a linear relation,

$$\mathbf{A}^{cv} \phi^{cv} = a_P \phi_P + \sum_N a_N \phi_N = \mathbf{R}^{cv}. \quad (2.21)$$

The coefficients a_P and a_N are calculated from values of current time state ϕ_i^n and the \mathbf{R} contain the previous time state. A loop over all cv in a given domain using a topological index mapping creates a sparse matrix relation,

$$\mathbf{A}[\phi^n] \phi^n \equiv \sum_{cv} \mathbf{A}^{cv} \phi^{cv} = \sum_{cv} \mathbf{R}^{cv} \equiv \mathbf{R}[\phi^{n-1}]. \quad (2.22)$$

In the case of a structured grid, where the cv become cubes, this scheme coincides with second order central difference FD scheme with semi-discretized implicit Euler scheme in time. Note that \mathbf{A} depends on ϕ_i , this non-linearity must be solved, and is termed pressure-velocity dependency. The procedure to solve Eqn (2.20) implies three such linear equations to be solved, where the flux interrelates all three. In order to define the solution procedure in icoDyMFoam [28, 65], the solver in OpenFOAM used for the fluid domain in this thesis, some definitions are needed. First the $\mathbf{H}[\mathbf{U}]$ operator,

$$\mathbf{H}[\mathbf{U}] = - \sum_N a_N \mathbf{U}_N + \frac{\mathbf{U}_P^o}{\Delta t}, \quad (2.23)$$

where U^o is rest term from Eqn (2.20) minus the pressure term. Then the explicit velocity correction becomes,

$$\mathbf{U}_P = \frac{\mathbf{H}[\mathbf{U}]}{a_p} - \frac{1}{a_P} (\nabla p)_P \approx \frac{\mathbf{H}[\mathbf{U}]}{a_p} - \sum_k \frac{1}{a_P} \mathbf{S}(p)_k. \quad (2.24)$$

By using Eqn (2.24) into the incompressible flow condition Eqn (2.16), the pressure equation is then obtained, a Laplacian solved by using Eqn (2.14) and Eqn (2.15),

$$\sum_k \mathbf{S} \cdot \left[\left(\frac{1}{a_P} \right)_k (\nabla p)_k \right] = \sum_k \mathbf{S} \cdot \left(\frac{\mathbf{H}[\mathbf{U}]}{a_P} \right)_k. \quad (2.25)$$

The BC, physical as well numerical (fluxes and interpolated face values) is implemented by explicit correction in the Eqn (2.22) and projection techniques, the details of these steps are omitted.

The pressure-velocity dependency is solved by Rhie-Chow interpolation in the following scheme, known as the PISO algorithm,

- Solve the \mathbf{U} , by solving the momentum predictor step using flux and pressure from previous time step in Eqn (2.22).
- Calculate $\mathbf{H}[\mathbf{U}]$ using Eqn (2.23).
- Update the flux \mathbf{F} using Eqn (2.24).
- Solve the pressure equation, Eqn (2.25).
- Update \mathbf{U} using Eqn (2.24).
- Repeat from second step until tolerance is reached in \mathbf{U} .

This assumes the coefficients in $\mathbf{H}[\mathbf{U}]$ in terms of previous time steps, hence changing the dependence of \mathbf{A} given in Eqn (2.22) from ϕ^n to ϕ^{n-1} ! The correction for this creates the PIMPLE algorithm which is simply a repetition of the PISO until convergence is achieved. The issue by this approximation is not further pursued in this thesis but details are given in the PhD thesis of Jasak [28].

2.5 Quasi-steady approximation

The quasi-steady approximation assumes that the structural response is in equilibrium with the fluid instant, using small strain assumption, with $\epsilon = \frac{1}{2}(\nabla + \nabla^T)$ and then the following constitutive relation is used,

$$\dot{\sigma}_{ij} = D_{ijkl} \epsilon_{kl}(\dot{\mathbf{q}}), \quad (2.26)$$

where D_{ijkl} is the tensor expression for linear elasticity and \mathbf{q} the displacement field. Using implicit Euler and multiply on both sides the Δt this becomes at given time step n ,

$$\sigma_{ij}^n = \sigma_{ij}^{n-1} + D_{ijkl}\epsilon_{kl}(\Delta\mathbf{q}^n), \quad (2.27)$$

inserting this into equation of motion Eqn (2.7) assuming $b_i = 0$,

$$\partial_j D_{ijkl}\epsilon_{kl}(\Delta\mathbf{q}^n) = f_i^n + \sigma_{ij,j}^{n-1}. \quad (2.28)$$

Rewrite this by using the divergence theorem starting with the LHS, taking the scalar product with test function ϕ over interior $\Omega = \Omega(t_{n-1})$. Define n_j the normal vector of the surface $\partial\Omega(t_{n-1})$ using that σ_{ij} is symmetric,

$$(\partial_j D_{ijkl}\epsilon_{kl}(\Delta\mathbf{q}^n), \phi_i)_\Omega = (n_j D_{ijkl}\epsilon_{kl}(\Delta\mathbf{q}^n), \phi_i)_{\partial\Omega} - (D_{ijkl}\epsilon_{kl}(\Delta\mathbf{q}^n), \epsilon_{ij}(\phi))_\Omega. \quad (2.29)$$

The RHS,

$$(f_i^n, \phi_i)_\Omega + (\sigma_{ij,j}^{n-1}, \phi_i)_\Omega = (f_i^n, \phi_i)_\Omega - (\sigma_{ij}^{n-1}, \epsilon_{ij}(\phi))_\Omega + (n_j \sigma_{ij}^{n-1}, \phi_i)_{\partial\Omega}. \quad (2.30)$$

Using the BC, $n_j D_{ijkl}\epsilon_{kl}(\Delta\mathbf{q}^n) = f_i(t_n) - f_i(t_{n-1}) = f_i - f_i^{n-1}$, zero displacement on $\partial\Omega_D$,

$$(D_{ijkl}\epsilon_{kl}(\Delta\mathbf{q}^n), \epsilon_{ij}(\phi))_\Omega = (f_i(t_n), \phi_i)_{\partial\Omega_N} - (\sigma_{ij}^{n-1}, \epsilon_{ij}(\phi))_\Omega. \quad (2.31)$$

where $\partial\Omega_D$ is the Dirichlet boundary, $\partial\Omega_N$ is the Neumann boundary. This is the bilinear form $a(\cdot, \cdot)$ for the structural part in Euler description for FEM. The complicated part is the need for calculate rotation matrix update of the second order stress tensor for each cell. For infinitesimal incremental step $\Delta\mathbf{q}^n$, the method holds for arbitrary deformations \mathbf{q}^n .

2.6 Weak form for static system of the solid state

The equation of motion, Eqn (2.7) applying the Newtons second law on RHS or use Eqn (2.6) with $\mathbf{U}=0$, in strong form can in tensor notation be formulated as,

$$\sigma_{ij,j} + b_i = \rho_s \ddot{q}_i. \quad (2.32)$$

Assume linear elastic constitutive law, using symmetric gradient $\epsilon = \frac{1}{2}(\nabla + \nabla^T)$ and displacement field \mathbf{q} ,

$$\sigma_{ij} = D_{ijkl}\epsilon_{kl}(\mathbf{q}). \quad (2.33)$$

The strong form then becomes

$$\rho_s \ddot{q}_i - \partial_j D_{ijkl}\epsilon_{kl}(\mathbf{q}) = b_i. \quad (2.34)$$

The static system is obtained by putting $\rho_s \ddot{q}_i$ to 0. By using isotropic approximation over the mesh domain Ω with Lamé parameter (λ, μ) , the D_{ijkl} can be defined as,

$$D_{ijkl} = \lambda \delta_{ij} \delta_{kl} + \mu (\delta_{ik} \delta_{lj} + \delta_{il} \delta_{kj}). \quad (2.35)$$

The partial differential operator from Eqn (2.34) of elliptic characteristic, acting on solution \mathbf{q} , can be described as a bilinear operator $a(\cdot, \cdot)$ within a finite sub domain V_n . This is obtained by multiplying the strong form with a trial function \mathbf{v} , integrate over a control volume then using the divergence theorem,

$$a(\mathbf{q}, \mathbf{v}) = (\lambda \partial_i q_i, \partial_j v_j)_\Omega + (\mu \partial_i q_j, \partial_i v_j)_\Omega + (\mu \partial_i q_j, \partial_j v_i)_\Omega. \quad (2.36)$$

This relation is used in the FEM approximation as described in the next section.

2.7 The Finite Element Method

In the Galerkin approximation, given a finite dimensional subspace V_n of the solution space V to the PDE satisfying the BC, then find the $\mathbf{q} \in V_n$ such as,

$$a(\mathbf{q}, \mathbf{v}) = (\mathbf{f}, \mathbf{v}), \forall \mathbf{v} \in V_n. \quad (2.37)$$

Expanding the displacement field \mathbf{q} by a set of test functions,

$$\mathbf{q} = \sum_k \mathbf{q}_k \tilde{q}_k \equiv \mathbf{N}_q \tilde{\mathbf{q}}. \quad (2.38)$$

and define the residual $\Phi = a(\mathbf{q}, \mathbf{v}) - (\mathbf{f}, \mathbf{v})$, where the \mathbf{v} is a trial function in V_n . The $a(\cdot, \cdot)$ depends upon the constitutive modelling. In this thesis Eqn (2.36) is used. The integration is performed over the cell N , $A_{ij}^N = a(\mathbf{v}_i, \mathbf{v}_j)_N$, and the summation of all contributing cells is denoted as the assemble of the stiffness matrix,

$$K_{ij} \equiv a(\mathbf{v}_i, \mathbf{v}_j) = \sum_N A_{ij}^N. \quad (2.39)$$

Each cell integration is approximated by Gauss quadrature, and isoparametric mapping. Given any function g , define the computational domain V_0 , the current domain by V and the Gauss quadrature points ξ_i . This implies a Jacobian for the deformation of the cell from computational domain to the current domain, and weight factor η_i related to the choice of quadrature points ξ_i ,

$$\int_V g(x) dV = \int_{V_0} g(\xi) \det J d\xi \approx \sum_i g(\xi_i) \det J(\xi_i) \eta_i. \quad (2.40)$$

In adaptive meshing, one has to ensure the condition of conforming elements [60] and in order to avoid linear dependence in $a(\cdot, \cdot)$, a constraint equation is formed to lock the freedom of the nodes which are on the edges of each element, the sub-cells, referred as to hanging nodes in the DEAL.II package [61].

The solution procedure is to minimize above residual $\Phi = 0$ which expressed in the basis of V_n becomes

$$\mathbf{K}\mathbf{q} = \mathbf{f}, \quad (2.41)$$

where \mathbf{q} is the displacement vector in the space spanned by the trial functions \mathbf{v} , \mathbf{K} is the stiffness matrix and \mathbf{f} the force vector. The setting of the trial functions as the displacement field functions based upon a given mesh gives the Finite Element Method (FEM). The BC of Dirichlet type is met by condensing the linear matrix, and the Neumann condition appears as traction elements in the \mathbf{f} vector.

2.8 Governing equation in the state space formalism

The strong form of the PDE for the Eqn (2.7) in state space,

$$\dot{q}_i - v_i = 0, \quad (2.42)$$

$$\rho_s \partial_t v_i + C_{il} v_l - \partial_j D_{ijkl} \epsilon_{kl}(\mathbf{q}) = f_i. \quad (2.43)$$

In state space, the structural dynamics for the undamped/[damped] system takes the following form,

$$\dot{\mathbf{q}} - \mathbf{v} = \mathbf{0}, \quad (2.44)$$

$$\mathbf{M}\dot{\mathbf{v}} + [\mathbf{C}\mathbf{v}] + \mathbf{K}\mathbf{q} = \mathbf{f}. \quad (2.45)$$

where [60],

$$\mathbf{K} = \int_{\Omega_s} (\nabla \mathbf{N}_q)^T \mathbf{D} (\nabla \mathbf{N}_q) d\Omega_s, \quad (2.46)$$

$$\mathbf{M} = \int_{\Omega_s} \rho_s \mathbf{N}_q^T \mathbf{N}_q d\Omega_s. \quad (2.47)$$

Here \mathbf{K} is same as previous section but slightly reformulated due to Eqn (2.36). Assuming the structural damping matrix \mathbf{C} ,

$$\mathbf{C} = \alpha \mathbf{M} + \beta \mathbf{K}, \quad (2.48)$$

known as Rayleigh damping, useful when the natural frequency is known. The damping is introduced by adding the $[\mathbf{C}\mathbf{v}]$ term to the equation in version 0.3 and thereby its distinction. By semi-discretization of the time variable in Eqn (2.44) and Eqn (2.45), $\hat{\mathbf{a}} = \frac{\mathbf{a}^n - \mathbf{a}^{n-1}}{\Delta t}$, and introduce blending by using the theta method, $\hat{\mathbf{a}} = \theta \mathbf{a}^n + (1 - \theta) \mathbf{a}^{n-1}$,

$$\mathbf{q}^n = \mathbf{q}^{n-1} + \Delta t \hat{\mathbf{v}}, \quad (2.49)$$

$$[\mathbf{M} + \Delta t \theta \mathbf{C}] \mathbf{v}^n = [\mathbf{M} - (1 - \theta) \Delta t \mathbf{C}] \mathbf{v}^{n-1} - \Delta t \mathbf{K} \hat{\mathbf{q}} + \Delta t \hat{\mathbf{f}}. \quad (2.50)$$

There are two ways of solving this, updating first \mathbf{v} and then \mathbf{q} gives the simplest equation to solve,

$$[\mathbf{M} + \Delta t \theta \mathbf{C} + \theta^2 \Delta t^2 \mathbf{K}] \mathbf{v}^n = [\mathbf{M} - (1 - \theta) \Delta t \mathbf{C} - \theta(1 - \theta) \Delta t^2 \mathbf{K}] \mathbf{v}^{n-1} - \Delta t \mathbf{K} \mathbf{q}^{n-1} + \Delta t \hat{\mathbf{f}}. \quad (2.51)$$

However, by multiplying the Eqn (2.44) by $[\mathbf{M} + \Delta t \theta \mathbf{C}]$ and replace the \mathbf{v}^n in Eqn (2.44) using Eqn (2.45) gives the second variant:

$$[\mathbf{M} + \Delta t \theta \mathbf{C} + \Delta t^2 \theta^2 \mathbf{K}] \mathbf{q}^n = [\mathbf{M} + \Delta t \theta \mathbf{C} - \Delta t^2 \theta(1 - \theta) \mathbf{K}] \mathbf{q}^{n-1} + \Delta t \mathbf{M} \mathbf{v}^{n-1} + \Delta t^2 \theta \hat{\mathbf{f}}, \quad (2.52)$$

$$[\mathbf{M} + \Delta t \theta \mathbf{C}] \mathbf{v}^n = [\mathbf{M} - (1 - \theta) \Delta t \mathbf{C}] \mathbf{v}^{n-1} - \Delta t \mathbf{K} \hat{\mathbf{q}} + \Delta t \hat{\mathbf{f}}. \quad (2.53)$$

These are the two forms of Roth's equation in matrix form used in this project. In the stationary case, when velocity goes to zero the two variants of semi-discretized equations are equivalent to the expected $\mathbf{K}\mathbf{q} = \mathbf{f}$. The implemented code using this set of equations is *DynamicElastic* for dynamic case, *StaticElastic* for the static system. Final note, semi-discretization is used to separate the time domain from the spatial domain in the discretization which enables the use of an efficient adaptive meshing, another procedure is to use the method of lines, which implies a decoupling of the PDE into a set of ODE requiring one mesh for each equation, hence adaptive meshing becomes more expensive.

2.9 ALE description and imposed BC

The FEM in this study is expressed in terms of the material description, with displacement field as a function of original grid, while the FVM of the fluid has the solution with respect the current grid, the Euler description, with the pressure and velocity expressed in current grid. The no-slip condition is applied to the moving wall, which gives the additional condition that the fluid cell adjacent at the boundary have the same velocity as the grid points of solid sharing the same face to given fluid cell ($\mathbf{U}_r = 0$). This implies that the grid points of the fluid move coherently with the points of the solid on the coupling boundary. The pressure of the adjacent cell has imposed zero gradient condition ($\nabla p, \mathbf{n}) = 0$ which implies pressure static condition, hence the isotropic stress tensor of fluid and pressure has the same direction but with opposite sign. The fluid also induce a drag originating from the deviatoric stress tensor which at given grid point is the applied traction with the included pressure. The strategy to solve this problem, is by applying the traction vector on the solid state and to the fluid impose the displacement on the boundary to the fluid and re-mesh the grid and re-interpolate \mathbf{U} and p . This leads to the Dirichlet-Neumann partition condition in Arbitrary Lagrange-Euler description for the staggered solution of the FSI problem, for more details see [33, 11]. The critical aspect, in combining the descriptions, using the benefits of both is the complicating feature of the additional effort to re-mesh the domain described by the Euler description. The re-mesh procedure in OpenFOAM is based upon the pseudo-solid displacement approximation, which has its direct consequence that it assumes the displacement to be described by a potential, that is a solution to a Laplace equation.

2.10 The Fluid-Structure Interaction

A monolithic formulation of the FSI in FEM serves the purpose to give a closed expression of the co-moved mass factor and present the frequency shift for a cantilever with forced vibration analysis on VIV response. A detailed description of the staggered algorithm using Dirichlet-Neumann partition technique is presented.

2.10.1 Monolithic FSI Problem

The Laplacian form in strong form of PDE in Eqn (2.17) allows the FEM approximation. For the purpose of study the added mass effect inducing frequency shift and amplitude response FSI in this section, assume the fluid under FEM approximation.

The mass effect of the fluid is to be derived. In the following, for simplicity of the equations, assume incompressible inviscid flow and ignore the convective term and the gravitational effect for the fluid. By further using incompressible condition to eliminate the velocity then the Helmholtz governing equation for INS of the pressure is obtained,

$$\nabla^2 p = 0. \quad (2.54)$$

Assert FEM solution to the problem,

$$\mathbf{p} \simeq \mathbf{N}_p \tilde{\mathbf{p}}, \quad (2.55)$$

$$\mathbf{q} \simeq \mathbf{N}_q \tilde{\mathbf{q}}, \quad (2.56)$$

and dropping the tilde henceforth. For the structure, assume no damping and neglect the viscous effect. Then the following system equations for the fluid-structure coupling is obtained [60, 46],

$$\mathbf{H}\mathbf{p} + \mathbf{Q}^T \ddot{\mathbf{q}} + \mathbf{f}^F = \mathbf{0}, \quad (2.57)$$

$$\mathbf{M}\ddot{\mathbf{q}} + \mathbf{K}\mathbf{q} - \mathbf{Q}\mathbf{p} + \mathbf{f}^S = \mathbf{0}, \quad (2.58)$$

where \mathbf{f}^S and \mathbf{f}^F contains the force boundary terms. The new terms in the dynamical system, is the coupling term $\mathbf{Q}\mathbf{p}$ involving traction vector $\mathbf{t} = p\mathbf{n}$ where \mathbf{n} is the fluid surface normal and the pressure term \mathbf{H} ,

$$\mathbf{Q}\mathbf{p} = \int_{\partial\Omega} \mathbf{N}_q^t \mathbf{t} d\Gamma, \quad (2.59)$$

$$\mathbf{H} = \int_{\Omega_f} (\nabla \mathbf{N}_p)^T (\nabla \mathbf{N}_p) d\Omega_f. \quad (2.60)$$

The matrices form the same bilinear functions described in the previous sections. By substituting the Eqn (2.57) into Eqn (2.58) gives the following structured equation to be solved,

$$(\mathbf{M} + \mathbf{Q}\mathbf{H}^{-1}\mathbf{Q}^T)\ddot{\mathbf{q}} + \mathbf{K}\mathbf{q} + \mathbf{Q}\mathbf{H}^{-1}\mathbf{f}^F + \mathbf{f}^S = \mathbf{0}. \quad (2.61)$$

The $\mathbf{Q}\mathbf{H}^{-1}\mathbf{Q}^T$ is known as added mass matrix, or co-moved mass, this is the frequency shift causing the structure to move slower. For the cantilever, there is an analytical solution [55] to this added mass matrix, the time period for the natural frequency,

$$T_r = \left(1 + \frac{1}{4} \frac{L}{D} \frac{\rho_f}{\rho_s}\right)^{\frac{1}{2}} T_v, \quad (2.62)$$

where T_v is the natural time period in vacuum. The VIV can be analyzed by forced vibration analysis. Starting from Eqn (2.58) neglecting the \mathbf{f}^S term, and inserting the forced vibration assumption $\mathbf{q} = \mathbf{q}_0 e^{-i\omega t}$ and $\mathbf{p} = \mathbf{p}_0 e^{-i\omega t}$, the forced fluid structured equations of the VIV then becomes,

$$\mathbf{q}_0 = (\mathbf{K} - \omega^2(\mathbf{M} + \mathbf{Q}\mathbf{H}^{-1}\mathbf{Q}^T))^{-1} \mathbf{Q}\mathbf{p}_0. \quad (2.63)$$

This is the structural response on forced vibration for the steady incompressible inviscid flow. As the forced vibration ω approaches to the natural frequency of the structure, resonance should be observed. At this point, VIV is obtained as setting $\omega = f$ and it is plausible to assume $\mathbf{Q}\mathbf{p}_0 \sim \Delta\mathbf{p}$, pressure difference across the transversal direction sides of the cantilever.

2.10.2 Staggered FSI algorithm

Given the problem defined in ALE description, also known as Dirichlet-Neumann partition [33]. Define F the solver for the fluid and S the solver for the solid. The sub-cycle in the staggered algorithm to solve the problem can then be formulated as,

- Solve $F(\mathbf{q}^{n+1}, t^{n+1}, \mathbf{v}^{n+1}) = \mathbf{f}^F$.
- calculate the fluid's traction vector $\delta\mathbf{T}$ on the coupled boundary applied as Neumann condition on force load $\mathbf{f}^S(t^{n+1})$. (Neumann transfer step)
- Solve $S(\mathbf{q}^{n+1}) = \mathbf{f}^S(t^{n+1})$.
- From the displacement field $\delta\mathbf{q}$, from solid grid, move the boundary of the fluid. (Dirichlet transfer step)
- Move the fluid mesh accordingly $\Delta\mathbf{q} = 0$. This is the pseudo-solid approximation applied to the fluid mesh.
- repeat above procedure until convergence achieved such that predicted displacement field is consistent with given pressure difference, that is $\tilde{f} = F(S^{-1}(F(\mathbf{f}^{n+1}))) = \mathbf{f}^{n+1}$ or $\tilde{\mathbf{q}} = S^{-1}(F(\mathbf{q}^{n+1})) = \mathbf{q}^{n+1}$.

The procedure of this kind is also known as a *strongly* coupled solver [13]. The solver has the option to use a *weakly* coupled method, that is only one iteration.

2.11 Acceleration of the convergence

This section concern with two basic schemes to accelerate the convergence of the fixed-point iteration in the strongly coupled staggered FSI algorithm.

2.11.1 Aitkens relaxation method

In order to stabilize the convergence in the sub-cycle, a relaxation procedure on the Dirichlet transfer step was introduced, a generalization of the secant method, where finding the root of scalar equation $f(x^*) = 0$ is achieved by the algorithm [1],

$$(x_{n+1} - x_n) = -\frac{(x_n - x_{n-1})}{(f(x_n) - f(x_{n-1}))}f(x_n). \quad (2.64)$$

Assume the existence of fixed point $x^* = g(x^*)$, then $f(x) = g(x) - x$ becomes the residual ($g(x_n) = x_{n+1}$),

$$\Delta x = \left[-\frac{(x_n - x_{n-1})}{((x_{n+1} - x_n) - (x_n - x_{n-1}))} \right] (x_{n+1} - x_n). \quad (2.65)$$

The new solution is then $x_{n+1} = x_n + \Delta x$, the factor within brackets is the measure of a scaling of the step. Define $x_{n+1}^* = g(x_n)$ and generalize the factor to n-dimensional space, introducing scalar dots instead of multiplication, and difference in denominator by norm,

$$\gamma_n = -\frac{(\mathbf{x}_n - \mathbf{x}_{n-1})}{\|(\mathbf{x}_{n+1}^* - \mathbf{x}_n) - (\mathbf{x}_n - \mathbf{x}_{n-1})\|^2} \cdot (\mathbf{x}_{n+1}^* - \mathbf{x}_n). \quad (2.66)$$

The underlying interpretation is that for an algorithm accurate to the first order, the differential residual gives an estimation of the second order correction. The Aitkens relaxation then becomes,

$$\Delta \mathbf{x} = \omega_{n+1}(\mathbf{x}_{n+1}^* - \mathbf{x}_n) + (1 - \omega_{n+1})(\mathbf{x}_n - \mathbf{x}_{n-1}). \quad (2.67)$$

The under relaxation factor is then modified for the next step as $\omega_{n+1} = \gamma_n \omega_n$. Then applied to FSI the ω_{n+1} is limited to an upper bound to achieve an under-relaxed step.

2.11.2 The ROM method

The previous iterative solution can be used both as precondition during the FSI cycle and to approximate the time steps by interpolated solutions of previous steps. This is known as reduced order model (ROM) [16]. Using the previous solutions, the local derivatives in the Taylor expansion are expressed by FD schemes or Gauss-Newton method, giving an estimate of the next step solution. In this study, since this was not of high priority, the simplest choice was implemented,

$$\mathbf{q}_{n+1} = 3(\mathbf{q}_n - \mathbf{q}_{n-1}) + \mathbf{q}_{n-2}. \quad (2.68)$$

The DynamicElastic have a routine implemented such that it calculates exactly 3 points then extrapolates a given number of consequent steps, note however within the FSI cycle this formula is used in all steps. A n-ROM method is referred to as a ROM using n previous steps.

Chapter 3

Implementation

The functionality of the DEAL.II [61] version 6.1 and OpenFOAM version 1.4.1 [65] packages will be explained.

3.1 The compilation

Here follows a short instruction how to compile the packages. First download the open source packages and install them accordingly to the individual help files. Then in constructing the case, starting with the template discussed in the user guide for the OpenFOAM with *wmake* as constructing script. Add under same catalogue the DEAL.II code encapsulated under a namespace in order to avoid name conflicts. Open the *option* file under the *Make* catalogue and add the necessary options/flags to be used in order to compile the DEAL.II. However, this is done in practice by trial and error using *wmake* iterative and including all missing links into the option file from the output of the failed compilation log file.

3.2 Main program ICOFSI

The fluid solver used in this thesis and described in the theory section is *icoDyMFoam* and the main program *icoDyMFoam.C*, located under the application section of the OpenFOAM 1.4.1 release, was taken as a template for the staggered algorithm described in section 2.7 and the PISO algorithm was enclosed as header *icoDyMFoam.H*. The *DEAL.II* code was enclosed into a separate class under the namespace *DynamicElastic* and a namespace *share* contained the common data as mapping index between the domains and the traction vector. The brackets [] in the pseudo code shows to which class in respective step is assigned to in the FSI algorithm. The evaluation of the traction vector was placed in the main function in version 0.9. An issue with the gnu g++ compiler prevented to use the template class as defined by standard C++. The solution to this is to define the class every time it is used. Earlier version than 0.7 used only the isotropic part of the tensor, the pressure axial on faces of *cv*.

ICOFSI PSEUDO CODE

```

Load Fluid Mesh

Loop over multiple solid objects
  Load Grid [ dealiiGrid class ]
  Define boundary condition [dealiiSetBoundaryIndicator]
  Load parameters [dealiiParameterHandler]
  Mapping between fluid and solid [InterGridMapping]

Loop over Time
  Adjustable Timestep
  ROM interpolation step [InterGridMapping]
  Repeat until convergence FSI cycle
    Dirichlet Transfer Step [AutoMesh]
    Solve Fluid [icoDyMFoam]
    Calculate Traction Vector [Section 3.3]
    Refine Mapping functions [InterGridMapping]
    Neumann Transfer Step [InterGridMapping]
    Solve Solid [DynamicElastic]
    Aitkens relaxation [DynamicElastic]
  Update
    Probes [dealiiProbes]
    Fluid mesh [AutoMesh]

```

A short description of the class and their functionality,

- `DynamicElastic`, FEM solver. The algorithm from section 2.6 with acceleration step from 2.8.
- `icoDyMFoam`, FVM solver, OpenFOAM INS solver in ALE description, described in section 2.2.
- `InterGridMapping`, handles the mapping between fluid and solid face centers, based upon proximity distance classifier, section 3.5.2.
- `AutoMesh`, assign displacement field vector from interpolated face center on solid onto the center of fluid.
- `dealiiParameter`, the input handler to `DynamicElastic`.
- `dealiiGrid`, read the grid from `msh` format or create hard coded mesh for the `DynamicElastic`.
- `dealiiSetBoundaryIndicator`, creates the Neumann and Dirichlet BC on the solid mesh.

3.3 OpenFOAM Package

The OpenFOAM package developed in object-oriented C++ is a CFD library tool to handle numerical solution of PDE using FVM. The moment predictor step Eqn (2.22) is evaluated using class *fvVectorMatrix* which discretize and distributes the operators specified within curled brackets, the code extracted from include file *UEqn.H* in *icoDyMFoam*,

```
fvVectorMatrix UEqn
{
    fvm::ddt(U)
    +fvm::div(phi,U)
    -fvm::laplacian(nu,U)
}
solve(UEqn== -fvc::grad(p));
```

where *fvm* class refers to the solution method, the Finite Volume Method, *fvm :: ddt* the discretization scheme for local derivative in time, *fvm :: div* as divergence operator discretized as described by Eqn (2.18), *fvm :: laplacian* solves the viscosity term using $(\nabla \cdot \nabla)$ using Eqn(2.15) and Eqn (2.18). The *fvc* is referred as the Finite Volume Calculus class, containing the interpolation schemes, in this case (CD). The discretization scheme is determined by input file. The following illustrates the transcription between theory and the OpenFOAM,

$A_i U_i = R_i$	<code>solve(UEqn == -fvc::grad(p))</code>
a_P	<code>AU=UEqn().A()</code>
$U = \frac{1}{a_P} H[U]$	<code>U=UEqn().H()/AU</code>
$\phi = S \cdot H[U]$	<code>phi=vc::interpolate(U)& mesh.Sf()</code>
$\nabla \cdot (\frac{1}{a_P} \nabla p) = \nabla \cdot (\phi)$	<code>fvm::laplacian(1.0/AU, p)==fvc::div(phi)</code>
$U = U - \frac{1}{a_P} \nabla p$	<code>U-=fvc::grad(p)/AU</code>

The package contains data types which enables a compact description of the physical variables and overloading techniques to allow a direct interpretation between a mathematical formula in PDE and coding context. This is the benefit of Finite Difference/FVM using collocated grids. The snippet below taken from ICOSFI main code illustrates the implementation of the second order tensor and interpolation technique, the original source of this code was extracted from *liftDrag.H* taken from the OpenFOAM community [65]. This is σ_{ij} part which acts as the traction to be transferred between the grids, see Eqn (2.8). The viscous traction follows by the second term in Eqn (2.9).

```
Foam::tmp<Foam::Field<Foam::Vector<double>>>
ViscousTraction = -nu.value()*
                U.boundaryField()[Patch].snGrad();
Foam::tmp<Foam::Field<Foam::Vector<double>>>
PressureTraction = p.boundaryField()[OpenFOAM_Patch]*
```



```

Density.value*
mesh.Sf().boundaryField()[Patch]/
mesh.magSf().boundaryField()[Patch];
Foam::tmp<Foam::Field<Foam::Vector<double>>>
Traction = PressureTraction+ViscousTraction;

```

The *snGrad()* function is the member function of *U* calculating the magnitude of the viscous part of the traction, the returned value *ViscousTraction* is the vector field *U* with magnitude of viscous force. Regarding the second term *PressureTraction*, the *Sf()* member function is the normal of the face center, *magSf()* is the length, the face area. Hence the normal unit vector of the face cell is computed times the pressure. The overloading technique of C++ allows the compact formulation of tensor algebra. The original article [27] for OpenFOAM is recommended for explaining the interface and the structure of the package.

3.4 DEAL.II package

The DEAL.II package, is a C++ implemented FEM library for solving Differential Algebraic Equation (DAE) systems, using adaptive mesh and efficient linear algebraic solver libraries as *PetScWrapper* and *Trilinos* both allowing MPI. In a comparative study [36] its strength were also its weakness. Because of its high modularity, there was no automatic tools, providing standard solvers, as OpenFOAM provides. Following the notation from the theory section, the following list creates the connection between the code and theory,

$a(\cdot, \cdot)$	system_matrix
f	system_rhs
$v_i(\xi_q)$	fe_values.shape_value(i,q)
ξ_q	fe_values.quadrature_point(q)
$ detJ(\tilde{\xi}_i) \eta_i$	fe_values.JxW(q)

The documentation of the code is extensive, with articles on the subject aiding in detail in the construction of the stiffness matrix, the correction for the non-conforming elements in the adaptive meshing and the use of multi-threading. The tutorial section on this forum explains the use of the package in executable programs named as *step-X*, where $X = 1, \dots, 33$. In similar fashion as for OpenFOAM, overloading techniques/member function is used to give an easy transcription between code and the weak form formulated in the theory section. The template used for *DynamicElastic* and *StaticElastic* is *step-18*, *step-8*, *step-11* *step-10* and *step-23*.

The DEAL.II functionality is exemplified by the following snippet code of the evaluation of the surface integral of traction vector defined in section 3.3,

$$\int_{\partial\Omega} \frac{1}{\rho_s} T \cdot v(x)_i dx \approx \sum_q \frac{1}{\rho_s} T(\xi_q) v(\xi_q)_i |detJ(\xi_q)| \eta_i. \quad (3.1)$$

The first loop extends over the faces of a given cell. The *boundary_indicator()* ==1, ensures the surface face is chosen, the *reinit(...)* member function initializes the values of all test functions related to given cell. The inner loop is over the quadrature points, which approximates the integral.

```

double invrho=1/rho;
const unsigned int n_face_q = face_quadrature_formula.size();
comp_i = fe.system_to_component_index(i).first;

for (unsigned int face=0;
     face<GeometryInfo<dim>::faces_per_cell;++face)
  if ( cell->face(face)->boundary_indicator() == 1 ) {
    index=cell->face_index(face);
    fe_face_values.reinit(cell,face);
    for ( unsigned int q=0;q<n_face_q;++q) {
      cell_rhs(i)+=
        invrho*
        shared::db[n_object]->get_traction(comp_i,index)*
        fe_face_values.shape_value(i,q)*fe_face_values.JxW(q);
    }
  }
}

```

The `comp_i` link the connection to the degree of freedom to which coordinate axis in the vector index. From this snippet,

```

system_matrix.copy_from(mass_matrix);
system_matrix.add(theta*time_step,C_matrix);
hanging_node_constraints.condense (system_matrix);
stiffness_matrix.vmult (system_rhs, solution_u_cur);
system_rhs *= -theta * time_step;
stiffness_matrix.vmult (tmp, solution_u_prev);
system_rhs.add (-time_step * (1-theta), tmp);
mass_matrix.vmult (tmp, solution_v_prev);
system_rhs += tmp;
C_matrix.vmult (tmp, solution_v_prev);
system_rhs.add (-(1-theta)*time_step, tmp);
system_rhs += forcing_terms;

```

the clear difference between OpenFOAM and DEAL.II is illustrated. The snippet corresponds to the construction of the system matrix and system vector in equation of motion for the velocity update, Eqn (2.50). The left hand side of the equation is formed by member function *copy_from* from `mass_matrix` followed by the vector/matrix addition *add* function. The *vmult* is the member function for the matrix-vector multiplication. The arguments within each (..) of the member function is the input and destination vector/matrix for *vmult* and scaling factor and destination vector/matrix for *add*. The handle of constraints is explicit in the coding. Careful considerations must be done for all detailed parts of MPI coding, and is required to be explicit in DEAL.II, while all these are hidden structures in OpenFOAM. The MPI was due to technical issue removed in version 0.3. The adaptive mesh use the Kelly Algorithm, described by reference within the tutorials.

3.5 InterGridMapping

3.5.1 Mapping functions

The implementation of the *InterGridMapping* class contain the key associative mapping functions $\chi_{s \rightarrow f}$, $\chi_{f \rightarrow s}$ between face centers \mathbf{x}_f of fluid mesh and the structure \mathbf{x}_s on the coupling surface $\partial\Omega$ on respective mapping for the transfer steps. A proximity distance classifier for the definition of these mapping functions is implemented,

$$\chi(\mathbf{x}_s)_{s \rightarrow f} = \{\mathbf{x}_f : \min_{\mathbf{x}_f \in \partial\Omega} (\|\mathbf{x}_s - \mathbf{x}_f\|)\}, \quad (3.2)$$

$$\chi(\mathbf{x}_f)_{f \rightarrow s} = \{\mathbf{x}_s : \min_{\mathbf{x}_s \in \partial\Omega} (\|\mathbf{x}_s - \mathbf{x}_f\|)\}. \quad (3.3)$$

3.5.2 Transfer step

The inverse distance interpolation was applied in Dirichlet transfer step,

$$\Phi(\mathbf{X}) = \sum_i \frac{\|\mathbf{X} - \mathbf{x}_i\|^{-1}}{\sum_k \|\mathbf{X} - \mathbf{x}_k\|^{-1}} \phi_i, \quad (3.4)$$

which provides an efficient and accurate weight formula. However, due to technical details omitted for the evaluation of the traction in the Neumann transfer, plain average of the field over the fluid faces *within* given solid face was performed,

$$\Phi = \frac{1}{N} \sum_i \Phi_i. \quad (3.5)$$

Chapter 4

The case study

The case is a velocity driven fluid domain of rectangular shape with cantilever(s) as a structure immersed and attached to the wall. All values are in SI units.

4.1 Beam theory of the cantilever

The dimension of the cantilever is $(1 \times 1 \times 10) \cdot D^3$. Using beam theory, the Bernoulli's kinematic assumption in an one-dimensional dynamical continuous system with cross section area A_t and centered path of line is applied [23]. The u_l states the deflection for uniformly applied traction force over the long-side, and u_t is the deflection by force tangential at the tip of structure. The formulas for these deflections are given as follows, where pressure difference between front and wake side of the cantilever is denoted as ΔP ,

$$u_t = \frac{FL^3}{8EI} = k_t \frac{\Delta P}{E}, \quad (4.1)$$

$$u_l = \frac{FL^3}{3EI} = k_l \frac{\Delta P}{E}. \quad (4.2)$$

The corresponding vibrational frequencies,

$$\omega^2 = \frac{(2\pi)^2}{T^2} = 12.36 \frac{EI}{A_t \rho_s L^4} \Rightarrow T = k_\omega \sqrt{\frac{E}{\rho_s}}. \quad (4.3)$$

The strain energy U_t associated with deflection for u_t ,

$$U_t = \frac{1}{2} u_t F = \frac{1}{6} \frac{F^2 L^3}{EI} = \frac{3EI}{2L^3} u_t^2 = k_u \frac{(\Delta P)^2}{E}. \quad (4.4)$$

4.2 The steady state response for a cantilever.

By rewriting the advection term in Eqn (2.6),

$$\mathbf{U} \cdot \nabla \mathbf{U} = \nabla \left(\frac{\|\mathbf{U}\|^2}{2} \right) + (\nabla \times \mathbf{U}) \times \mathbf{U}. \quad (4.5)$$

Take Eqn (2.6) and drop time derivatives and viscosity term, apply then the Eqn (4.5) assuming no vorticity ($\nabla \times \mathbf{U} = 0$),

$$\rho_f \nabla \left(\frac{\mathbf{U} \cdot \mathbf{U}}{2} \right) = -\nabla p. \quad (4.6)$$

This is Bernoulli's equation for a steady irrotational inviscid flow. By integrating along a streamline,

$$p + \rho_f \frac{\mathbf{U} \cdot \mathbf{U}}{2} = C, \quad (4.7)$$

Assume uniform velocity profile over the structure in front of the cantilever, the static pressure as a function of the flow direction and small deflections. The argument is as follows, by applying the Bernoulli's relation on the stagnation point for the cantilever at rest, the fluid element adjacent to the cantilever where all dynamic pressure is transformed into pressure. Since the cantilever is allowed to move, the no-slip asserts the fluid cell shall move with the speed of the cantilever. The actual energy transferred to the cantilever is reduced by the amount of energy required to keep the fluid cell moving at given velocity, this is given by Eqn (4.7). This applied to the amplitude response for the cantilever Eqn (4.1) gives the relation between amplitude A by the flow using the moving fluid cell, with average speed of $2Af_n$, adjacent to the structure,

$$A = \alpha k \rho_f U^2 \frac{1}{1 + \sqrt{4U^2 k^2 \rho_f^2 f_n^2 + 1}}, \quad (4.8)$$

where α is a function of Re and the structure, a form factor. The dependence in Re arise from the proportionality between front pressure and the differential pressure over the structure. However α also depends on the size of the wake, which is a function of the form of the structure and the Re in the fluid. The f_n can without changing the equation become forced vibration ω .

4.3 Boundary condition

In OpenFOAM, BC is denoted as *patch*. The walls are no-slip, $\mathbf{U}_r = 0$, *movingWallVelocity* is the patch to be used for the coupled boundary and *fixed* for the other walls. Static pressure condition is enforced on all patches but the outlet, that is $(\nabla p, \mathbf{n}) = 0$, *zeroGradient*. The inlet has *fixed* for \mathbf{U} , that is Dirichlet condition. The outlet has *fixed* p , that is Dirichlet pressure ($p = 0$) and \mathbf{U} *zeroGradient*, $(\nabla \mathbf{U}, \mathbf{n}) = 0$. The setup of BC implies a velocity driven flow. These were the recommended settings taken from [28, 65]. The BC for the DEAL.II is automatic, in the sense use the proximity distance classifier in calculating the distance of given solid face center to the coupled boundary fluid and defines Neumann if within given tolerance and Dirichlet with zero displacement otherwise. The reason for not using the same system as OpenFOAM is that the topology is recalculated at loading/construction of the grid, an unfortunate feature of DEAL.II. It has been noted that the tolerance setting can be complicated by the shape of the surface and could create mismatched BC but as far the fluid cells exceed the number of solid this lower the chance this event.

4.4 Single cantilever study

The case study was taken from [53], the thickness of the cantilever is $D = 0.2$ m and the height is $10D$, placed $5D$ from inlet and $2.5D$ from the walls while the outlet is placed $20D$ from the cantilever. The wire frame of the rectangle domain is thus $(26 \times 6 \times 12.5) \cdot D^3$.

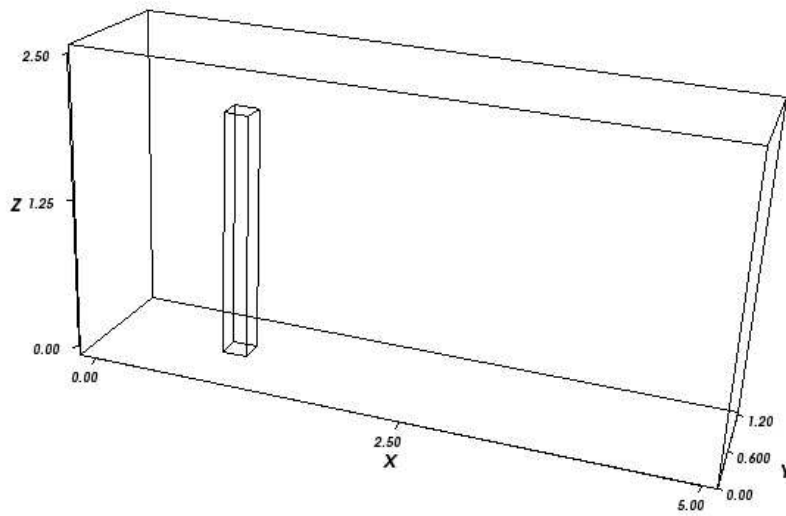


Figure 4.1: single cantilever case study.

4.5 Multi-block cantilever study

The multi-block case is similar to the single cantilever case, but with four cantilevers where distance between them is $1D$, thus giving a wire framed rectangle of size $(28 \times 8 \times 12.5) \cdot D^3$. The case originated from a multi cantilever study [50].

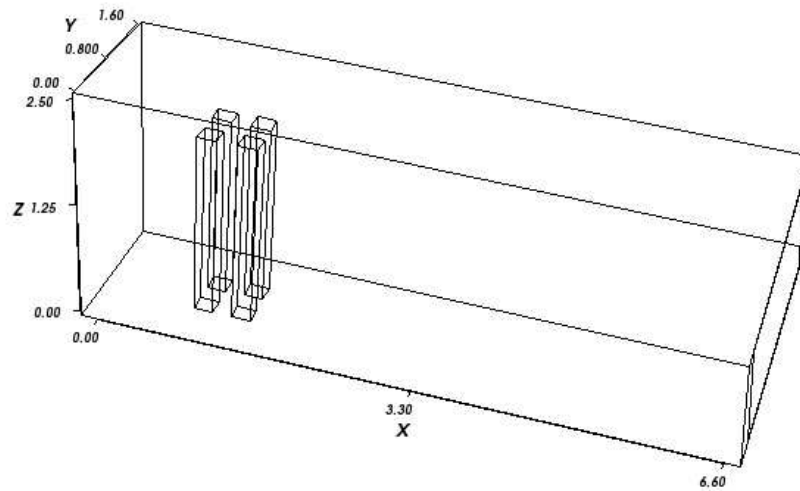


Figure 4.2: The multi cantilever case study.

4.6 The cantilever mesh

The DEAL.II mesh have some support for generate mesh. A simple structure was desirable requiring a small code to generate the mesh in DEAL.II and then saved as gmesh format. The mesh was then to be loaded during the FSI simulation. The simplicity in building this cantilever mesh was therefor an incentive in chosing this application to the validate the algorithm. The original mesh is 4x4x16 cells, see left Figure 4.3. The refinement procedure is done by dividing each cell into four cells, where the Kelly algorithm [30] is used in applying the criteria for this adaptive meshing. In same way coarsening is performed, the refined mesh contain information on coarser mesh, hence the coarsest mesh cannot be coarser. The loop over such refinement defines the number of steps taken. It has very close connection to the pseudo solid displacement step in the FSI algorithm. The right Figure 4.3 gives the 8x8x32 cell structure after one refinement. A more elaborate adaptive meshing is given in tutorial step-14. The settings of the Kelly algorithm, is the same as those given in tutorial step-8.

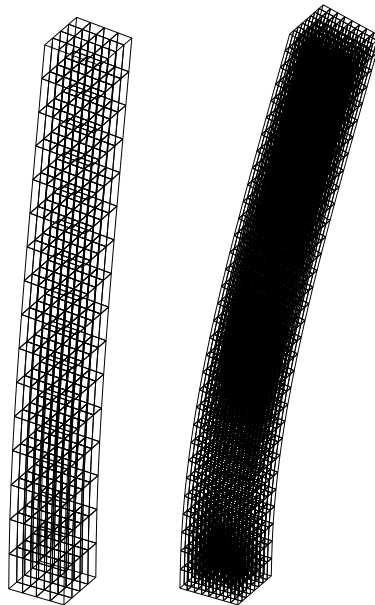


Figure 4.3: left initial mesh, right mesh after one refinement. The mesh is taken from simulation at different times

The class which perform this action is *coarse_and_refine*, the parameters of tolerance is a value obtained after a numerous testing within the community and developers of the package [61]. The *Gmesh* utility [75] can be used in constructing a mesh of the cantilever, see further details from the forum in how to define the grid, note that *Gambit* also have the option to construct readable input mesh, however, no effort have been done to investigate this further.

4.7 The fluid domain mesh

The mesh is generated by Gambit version 2.4.6 using scaled tetrahedral elements, with a structured mesh on the coupled boundary of cell size 0.02 m, growth rate 1.1 and 0.1 m as upper limit on cell diameter. Figure 4.4 shows the mesh around the cantilever. The *checkMesh*

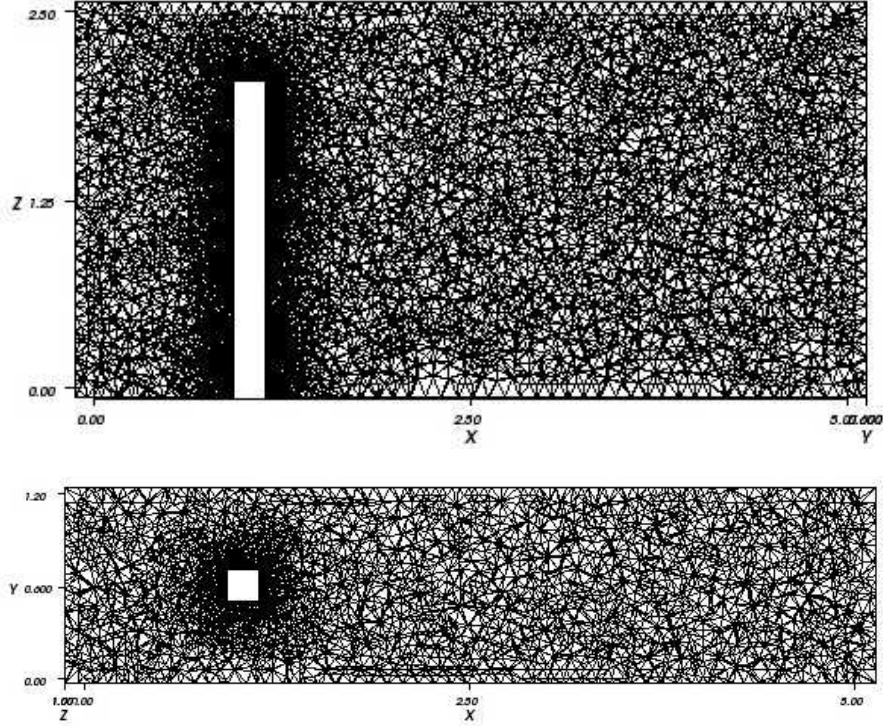


Figure 4.4: The mesh in XY at Z=1 m and XZ at Y=0.6 m.

post-Processing utility using the quality rules provided by the OpenFOAM community gives the result that grid is acceptable however there was an indication of stretched elements, within range of acceptance as long as one chooses a correct discretization and tolerance. There can be seen a clear change in orientation of *cells* in an area around the cantilever caused by the cap and this could implicate an area of conflict since flux goes in a different direction and hence introduces a non-orthogonality issue in the correction for the CD formula presented in the theory section where it is known to cause instability.

Chapter 5

Validation procedure

Each step of the algorithm is validated separately. The solid state is verified against beam theory. The mapping functions in the transfer steps and their interpolation is verified by direct an evaluation on test case and a check is performed at each simulation. The FSI algorithm is verified against frequency shift and amplitude equation.

5.1 Solid state solver

5.1.1 Test Case

The DEAL.II package support quadratic elements, cubes and square cells, although the number of quadrature points is an optional feature in this code, as well as the order of finite element basis, allowing under-integration respective nonlinear effects. These are features not fully exploited in this work, but the thesis [19] implements a technique useful to eliminate volumetric- and shear-locking as the Poisson ν approaches its upper bound limit 0.5. The non-linear trial functions increase the number of elements to such a degree that the current mapping function from face center of fluid to solid is not a viable option, since the size of number of degrees becomes too large. The test case is the same cantilever used in the FSI study with prescribed pressure on dedicated areas, long-side and short-side. Only linear elements are therefore considered and exact integration is used. The adaptive meshing is performed only once, using the Kelly Algorithm, with the argument that the study concerns steady PDE. The purpose is to study small deformations and therefore it is plausible to assume the traction is the same within a small perturbation. The benefit from this is that the stiffness matrix and the mass matrix is then calculated only once during a simulation. The actual update is very efficient, the cost lies in the mapping function between the fluid and solid. The refinement is controlled by an iterative update scheme where the cell is refined if the residual $\Phi = (\mathbf{K}\mathbf{q} - \mathbf{f})$ criteria is not fulfilled, and even coarsened if the residual is to small. In this way, it has been noted that the refinement allows you to construct a coarse or fine mesh but both lead to the same mesh after the iterative procedure coarse and refinement. The following code was used to test the class *StaticElastic*.

```

#include "InterGridMapping.H"
namespace shared
{
InterGridMapping<3>* icofsi_db_list[10] ;
InterGridMapping<3> icofsi_db;
}
#include "StaticElastic.H"
#include "dealiiGrid.H"
#include "setBoundaryIndicator.H"
#include "dealiiParameterHandler.H"
int main(int argc,char* argv[]) {
    shared::icofsi_db_list[0] = new InterGridMapping<3>();
    dealiiParameterHandler::Base prm(argv,"object0.prm");
    prm.print();
    int refinement=0;
    dealiiGrid::Grid<3> newGrid;
    SmartPointer<Triangulation<3> > tria;
    newGrid.create_grid();
    tria=newGrid.get_triangulation();
    StaticElastic::TopLevel<3> solver(prm,tria,refinement);
    solver.set_grid_path(argv,"object");
    solver.run();
}

```

5.1.2 Verification of class StaticElastic

Using the cantilever as case, with coarse grid and refine 0-2 gives a mesh with $16 \times 4 \times 4$, $32 \times 8 \times 8$ respectively $64 \times 16 \times 16$ cells taking linear trial functions and exact integration. The applied traction is $1Pa$, $E = 20 \cdot 10^3 Pa$, $I = \frac{1}{7500} m^4$, and the result u_c is compared to reference u_r from Eqn (4.2) and Eqn (4.1) with relative error $|\frac{u_c - u_r}{u_r}|$. The reference article

cells	256	2048	16384	Relative Error(%)
u_l/m	0.1285588	0.1441502	0.1488933	0.73
u_t/m	0.03430288	0.03844592	0.03968957	0.77

Table 5.1: The deflection u_t/u_l for StaticElastic

use $10 \cdot 10 \cdot 100 = 10000$ elements giving a error of 1.73% [53] for a FVM solver using Green-Cauchy strain measure.

5.1.3 Verification of class QuasiElasticity

The quasi-steady approximation is implemented as class *QuasiElasticity* and corresponds to a rewrite of the step-18 tutorial in DEAL.II with MPI removed and the code with traction vector taken from step-12. The validation of this routine is excluded from this report due to its limited use but for certain cases such as those in the VIV section presented, this routine

is suitable. The reason for its presentation in the thesis is due to the observation of fluid driven motion in VIV where steady state is entered in the first cycle and that an article on the subject presented a condition for the applicability of the method in terms of Keulegan Carpenter Number (KC) [5] which describes the relative importance of the drag force and the inertia forces. For lower numbers the inertia dominates. In order for this approximation to be valid, drag force must dominate over inertia, which is from a physical point of view intuitive. The StaticElastic is the stripped version of QuasiElasticity and the same testing was performed. The major difference is that StaticElastic is in Lagrange description, while QuasiElasticity is in Euler description. This solver was used in version 0.1.

5.1.4 Verification of the class DynamicElastic

The test code used for this class was,

```
#include "InterGridMapping.H"
namespace shared
{
  InterGridMapping<3>* icofsi_db_list[10] ;
  InterGridMapping<3> icofsi_db;
}
#include "DynamicElastic.H"
#include "dealiiGrid.H"
#include "setBoundaryIndicator.H"
#include "dealiiParameterHandler.H"
int main(int argc,char* argv[]) {
  shared::icofsi_db_list[0] = new InterGridMapping<3>();
  dealiiParameterHandler::Base prm(argv,"object0.prm");
  prm.print();
  SmartPointer<Triangulation<3> > tria;
  dealiiGrid::Grid<3> newGrid;
  newGrid.set_path(argv,"object");
  newGrid.create_grid();
  tria=newGrid.get_triangulation();
  DynamicElastic::TopLevel<3> solver(prm,tria,i);
  solver.set_grid_path(argv,"object");
  double time=0;stop=1;
  while(time<stop) {
    solver.set_current_time(time);
    time+=0.001;
    solver.run();
    solver.next_step();
  }
}
```

The dynamic solution is characterized by the amplitude and frequency. To given material constants and time steps in this test case, the order of accuracy is 10^{-8} . After 40-75 cycles (~ 1000 iterations in total with fixed-point iteration) only the last digit was changed in

energy, this was repeated for different densities ρ_s . The test was performed at version 0.5, using the more complicated set of update solving two linear equations Eqn (2.52) and Eqn (2.53). In version 0.8 the first update scheme was chosen, no difference is noted. The test revealed shear-locking when applying the traction on the tip of the cantilever, the longitudinal waves induced by the impact reflects from the base of the cantilever in twisting mode. For this reason, the traction was applied on the long-side. The same settings as the static system, the time period, T_p , for different mesh, can be obtained from the output files directly, as the turning points, maximum deflection or equivalent, when the kinetic energy is at minimum. The "Maximum Displacement VECTOR" in the output was introduced as to confirm the vibrational turning point and at same time confirm the coupling to the kinetic energy. The result of time periods T_c is compared to the Eqn (4.3) with relative error $|\frac{T_c - T_r}{T_r}|$, The error

cells	256	2048	16384	Error(%)
$T_{0.01}/s$	0.081	0.086	0.088	<0.5
$T_{0.1}/s$	0.255	0.272	0.277	< 0.5

Table 5.2: Periods from DynamicElastic.

in turning point is ± 1 ms, due to that the time step is 1 ms. The frequency implicates that K and M is implemented correctly into Roth's equation but it remains to show that the force contribution to the equation is correct. This is done by introducing damping to the system. The test is performed on the smallest system $16 \times 4 \times 4$, using the same contribution from mass and kinetic (ie $\alpha = \beta$) in percent expressed, 5% respective 1% and the time step changed to 0.01 s. The expected feature is that velocity is damped until it reaches zero then the solution shall become the same as for static according to the Eqn (2.50) after rearranging the terms. Figure 5.1 summarize the outcome.

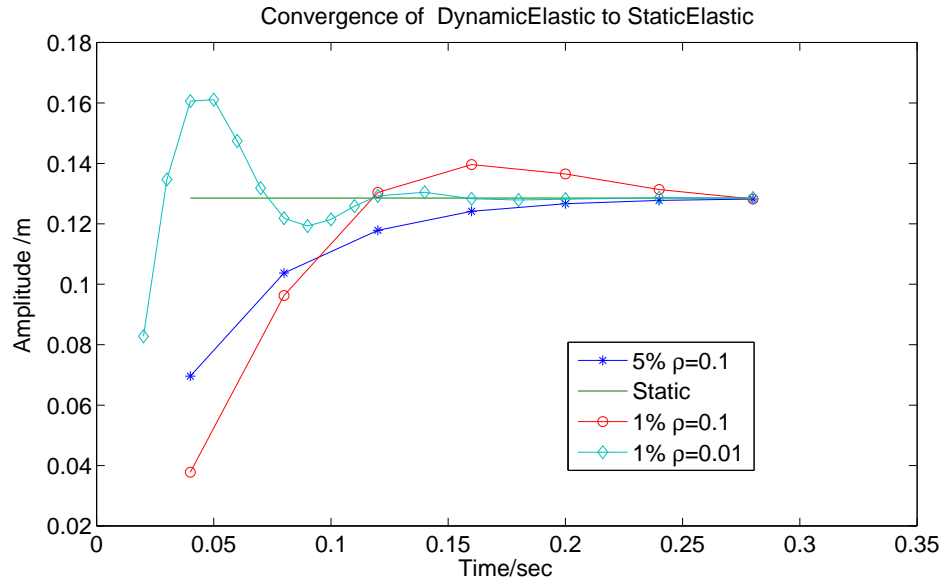


Figure 5.1: A critical damped dynamical system 0-0.30 s

5.2 icoDyMFoam

The verification of the stand alone solver icoDyMFoam itself is considered as performed within the community of OpenFOAM, this case is the central case in 2006 release of OpenFOAM with over two years testing with numerous articles and reports as result. The misconception however in using a code that is not properly documented have its consequence as [44] set improper patches, that is BC. This can also been seen in the FSI solver *icoStructFoam* distributed within the OpenFOAM forum. The *MovingWallVelocity* and *calculated* patch are vital in order for that the solver to work as intended.

5.3 setBoundaryIndicator and InterGridMapping

The auxiliary class setBoundaryIndicator uses the same proximity distance classifier to define the BC as used in transfer steps, hence this class is verified in the same step as InterGridMapping is verified. This distance classifier is the key function that keeps the grid together. Therefore in every run a sanity check is performed without any extra cost for each run. In the log file the tags "Max distance FOAM2DEAL" and "Max Distance DEAL2FOAM" gives the maximum distance in the into maps $\chi_{f \rightarrow s}$ and $\chi_{s \rightarrow f}$, that is $\max_{\mathbf{x}_s \in \partial\Omega}(\min_{\mathbf{x}_f \in \partial\Omega}(\|\mathbf{x}_s - \mathbf{x}_f\|))$ resp $\max_{\mathbf{x}_f \in \partial\Omega}(\min_{\mathbf{x}_s \in \partial\Omega}(\|\mathbf{x}_s - \mathbf{x}_f\|))$. For all calculations performed, this was confirmed valid as giving the distance within half a cell size of respective mesh *except* for one situation. This confirms the functionality of the proximity distance classifier. The *InterGridMapping* was verified further by placing two identical squares adjacent with different structured mesh generated by respective solver and by hand control the results in the printout list. In the log file there is a printout in the number of faces with Dirichlet and Neumann. The result is verified as well giving the expected number of faces for each type of condition.

The situation observed was a glitch in the restart of the simulation, discontinuities of the order of the cell size due to imperfect match between fluid and solid. This is an error that can be estimated by knowing the value of the gradient of ϕ over the cantilever and the cell size. The problem arise whenever a given point \mathbf{X} is on the border line between two cells. The estimation of the face centers in the Euler description of the solid as the *average* of surface vertices gives a discrepancy between fluid and solid which can cause a mismatch in the mapping function and indirectly cause a jump in the displacement from the misplaced traction vector since the topological mapping is lost and has to be recomputed at the restart, a unfortunate feature of DEAL.II.

5.4 The FSI algorithm

InterGridMapping is verified as to mapping the traction of the fluid to the correct position in the solid, and the displacement of the solid to correct position of the fluid. The same applies for the topological settings, ie boundary condition, performed by *setBoundaryIndicator* class. The *icoDyMFoam* and *DynamicElastic* solver are verified. The objective that remains is to ensure that FSI is implemented correctly. The verification steps are as follows,

- The shift in time periods is compared to theoretical values.
- The amplitude is related to the formula postulated in this thesis.
- The margin of error is not increased with FSI.

5.4.1 Setup

The single cantilever case, described in section 4.4 was used and using the BC settings from section 4.3 and mesh generated by Gambit as described in section 4.7. All initial data within the grid are zero and *icoDyMFoam* is performed until steady state is reached. This is defined as flow volume ten times the domain volume according to the User Guide of OpenFOAM downloaded from [65] with a $Co=0.5$. However, during the FSI simulation, $Co = 0.9$. This is a questionable choice since in the forum of OpenFOAM it has been pointed out that for stability issue using adjustableTime step, $Co < 0.5$ is recommended. However, due to the time limit of this project, the speed of the simulation was increased by using $Co=0.9$. Three different velocities were chosen at the inlet patch, $U = 1, 10, \text{ resp } 25 \text{ ms}^{-1}$. The Reynolds number ($\frac{UD}{\mu^*}$) is set to 400 and hence giving the kinematic viscosity μ^* as $5 \cdot 10^{-4}, 5 \cdot 10^{-3}, \text{ resp } 12.5 \cdot 10^{-4} \text{ m}^2\text{s}^{-1}$. The cantilever use the $32 \times 8 \times 8$ mesh with 2048 cells, $E = 20 \cdot 10^6$ Pa and Poisson number $\nu = 0.3$. In this study marker point it is placed at the center of tip of the free end of the cantilever. The tolerance is set to $1 \cdot 10^{-6}$ for the pressure and velocity in the *icoDyMFoam*, three PISO loops, the displacement in AutoMesh to $1 \cdot 10^{-6}$, the tolerance for the Aitkens acceleration $1 \cdot 10^{-7}$ and convergence criteria $1 \cdot 10^{-12}$ for the CCG solver of the linear system in FEM. Finally, the Crank-Nicholson scheme was chosen in the temporal discretization by setting $\theta = \frac{1}{2}$.

5.4.2 A note on measurement of the period

In the forthcoming tables, *Period* refers to how many periods a given marker point is evolved during the simulation, and the reason for this is to present how the time period was measured. In table 5.3, T_{p_i} refer to the time of the peak p_i in total amplitude with respect to original mesh. T_c is the estimated time of period. FFT refer to the DFT routine in MATLAB for the

Period	T_c	Error(%)
0.5	$2 \cdot T_{p_1}$	<20
0.75	$2 \cdot (T_{p_1} - T_{p_2})$	<10
1-10	$T_{p_n} - T_{p_{n+2}}$	<5
>10	FFT	0

Table 5.3: The measure of T_c .

discrete Fourier analysis. The error is the estimated relative in percent to the FFT obtained

for >10 period simulations, where it was assumed the DFT gave the exact result and transient effect was estimated. The in-line driven oscillation have *unknown* equilibrium point and by Figure 5.2 there is a transient movement before stationary orbit is entered, showing an initial movement in the direction of X then due to the VIV the orbit is created as going in an ellipse path. FFT was necessary in order to study VIV and higher frequencies in the marker points of the cantilever.

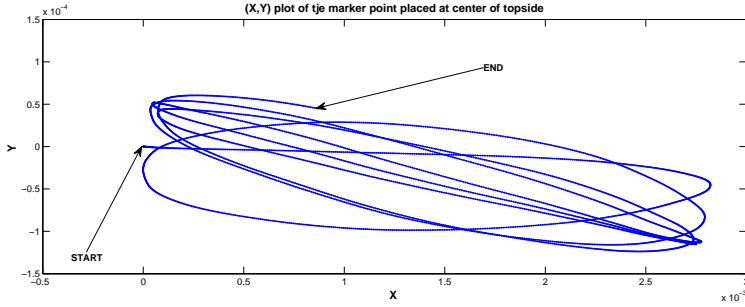


Figure 5.2: The trajectory of marker point position in XY space relative its reference point. The marker rapidly along X with a slow motion in Y direction, implicating the fluid lower frequency (Y) and the in-line motion of the natural frequency (X).

5.4.3 Result

T_v is the theoretical value of the time period given by Eqn (4.1) in vacuum. T_c is evaluated according to table 5.3 in the previous section. The T_r in the table is evaluated time period using Eqn (2.62) from [55]. For this reason the frequencies are not given in the tables. The deviation Dev refers to the relative error of T_c to this T_r , that is $|\frac{T_c - T_r}{T_r}|$. The A is the magnitude of the displacement field at marker point. The numerical error expressed in Dev have its origin in the quality of the mesh, the transition, the boundary conditions and the wall effect [40]. Using table 5.4 making the following optimization using least square,

$$T_c^2 = (A + B \frac{\rho_f}{\rho_s}) T_v^2 + C, \quad (5.1)$$

gives the result $A=1.74$, $B=2.54$ and $C=-0.004$. Higher order in relative mass had no influence. The theoretical value is $A=1$, $B=2.5$ and $C=0$ in accordance to Eqn (2.62). Applying this formula for the tables 5.4-5.6 gave the result in Figure 5.3. The first eight points from the left is from table 5.4, the seven to fifteen is from table 5.5 and the rest from table 5.6. The reason to optimize over a limited data is that the study of T^2 require adequate of points covering the whole range and evenly distributed. This is not possible for $U=10$ and 25 ms^{-1} due to limited time of the project to use only one processor per simulation and which in turn limits the study to short time periods to be used in the optimization, alsowhen taking the transient effect in account. The grid itself show areas which probably with time will cause divergence, mostly manifested at higher velocities as Figure 5.14 show. The frequency for the in-line driven motion should not to given Re depend on the actual flow speed and Figure 5.6 illustrates this with a standard deviation of $2.6 \cdot 10^{-3} \text{ s}$, note however the system is damping differently between cases and hence some slight difference is obtained. Furthermore, in the case of $\frac{\rho_f}{\rho_s} \ll 1$, the proportionality of the shift in frequency between different solid mass should be directly related to the vacuum. Figure 5.5 illustrates the correct scaling of a factor

of $\sqrt{5}$ which follows by Eqn (4.3) with a relative difference of 0.8%. The observed damping at $1 \cdot 10^{-2}$ m region is the area where the current time window of study damp the in-line and lift up the VIV unless the energetic loss drain the movement, and thus implying the lower amplitudes to be close early to the steady state and above, more simulation time is required to notice the effect. One significant result is the accurate correlation with the in-line amplitude with the proposed Eqn (4.8) showed in Figure 5.4. Figures 5.7-5.12 is the end time of the simulation, *not* the maximum amplitude.

ρ_s/kgm^{-3}	ρ_f/kgm^{-3}	T_v/s	T_c/s	T_r/s	A/m	Dev(%)	Period
2949	1000	1.0632	1.7442	1.4452	0.20	17	0.5
100	1000	0.1958	1.026	0.9983	0.17	3.7	0.75
50	1000	0.1384	1.016	0.9886	0.17	3	0.75
300	100	0.339	0.5840	0.4591	$1.4 \cdot 10^{-2}$	21	>10
300	200	0.339	0.6813	0.5537	$2.8 \cdot 10^{-2}$	19	6
10	0.01	0.0619	0.0864	0.0862	$2.5 \cdot 10^{-6}$	<1	> 10
50	0.01	0.1384	0.1940	0.1388	$2.6 \cdot 10^{-6}$	29	> 10
10	1	0.0619	0.0880	0.0692	$1.4 \cdot 10^{-4}$	21	> 10

Table 5.4: $U=1 \text{ ms}^{-1}$ $\text{Re}=400$, $E=20 \cdot 10^6 \text{ Pa}$, $\nu=0.3$.

ρ_s/kgm^{-3}	ρ_f/kgm^{-3}	T_v/s	T_c/s	T_r/s	A/m	Dev(%)	Period
10	0.1	0.0619	0.0863	0.0627	$2.8 \cdot 10^{-3}$	27	>10
10	20	0.0619	0.1509	0.1516	0.33	< 1	0.75
50	0.1	0.1384	0.1902	0.1382	$2.8 \cdot 10^{-3}$	27	>10
50	20	0.1384	0.2092	0.1958	0.37	10	1.5
100	20	0.1984	0.2667	0.2398	0.39	19	0.75
10	1	0.0619	0.0914	0.0692	$1.8 \cdot 10^{-2}$	24	8
5	20	0.0438	0.1480	0.1452	0.32	2	0.5

Table 5.5: $U=10 \text{ ms}^{-1}$, $\text{Re}=400$, $E=20 \cdot 10^6 \text{ Pa}$, $\nu=0.3$.

ρ_s/kgm^{-3}	ρ_f/kgm^{-3}	T_v/s	T_c/s	T_r/s	A/m	Dev(%)	Period
50	0.25	0.0619	0.1927	0.1384	$4.3 \cdot 10^{-2}$	28	3
10	0.1	0.0619	0.0861	0.0627	$6.4 \cdot 10^{-2}$	23	7
10	3.2	0.0619	0.0908	0.0831	0.38	8	1.25
50	3.2	0.1384	0.1947	0.1491	0.43	23	0.5
100	3.2	0.1984	0.2666	0.2035	0.45	24	0.5
10	1	0.0619	0.0879	0.0692	0.15	23	2.5
10	2	0.0619	0.0923	0.0758	0.26	18	0.5
1000	1	0.6191	0.8192	0.6199	0.17	24	0.5

Table 5.6: $U=25 \text{ ms}^{-1}$, $\text{Re}=400$, $E=20 \cdot 10^6 \text{ Pa}$, $\nu=0.3$.

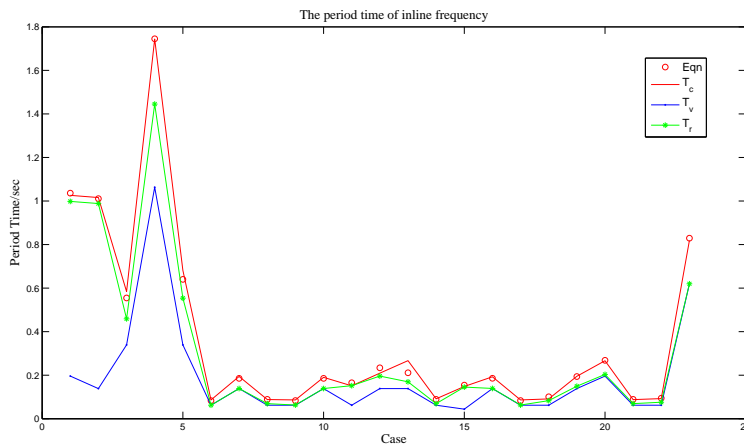


Figure 5.3: Periods for 23 Cases. The upper line is the measured points, the circles is the values predicted by Eqn (5.1) which is computed by least square to Table 5.4. The middle line (*) is the predicted values from Eqn (2.62) with vacuum values using Eqn (4.3) as the bottom line.

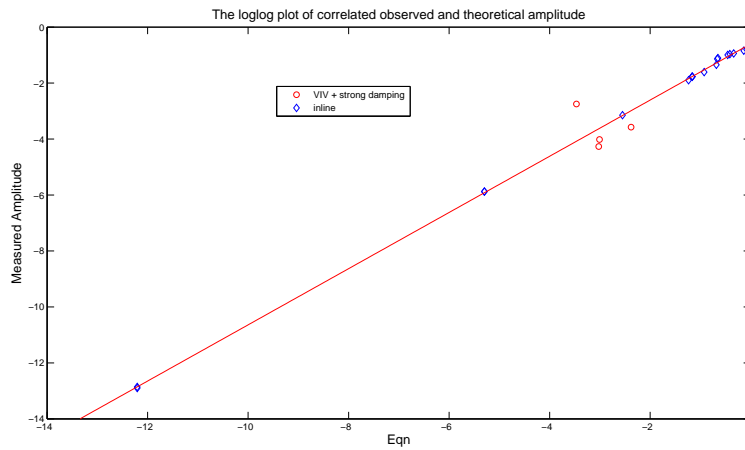


Figure 5.4: The correlation between dynamic pressure and deflection. The measured total magnitude amplitude v.s. Eqn (4.8). The slope is the form factor. The deviation is only for case where strong VIV have large influence on the data (o).

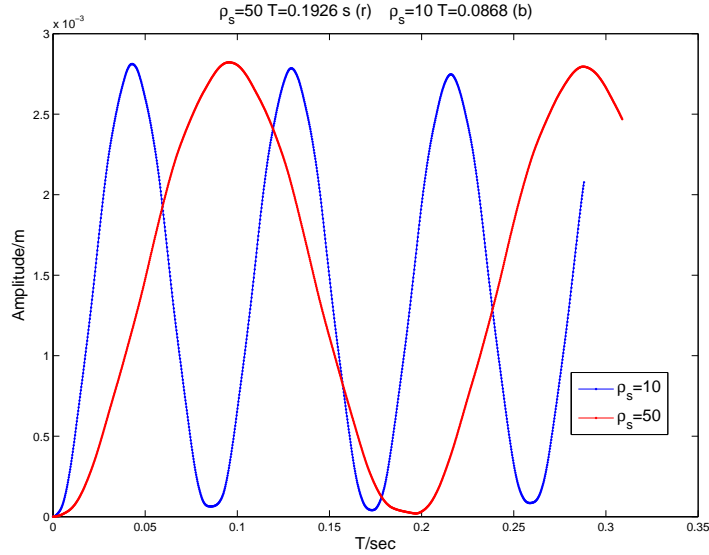


Figure 5.5: The magnitude amplitude of marker point placed at center of the tip. The scaling between case with low relative mass for $\rho_f = 0.1 \text{ kgm}^{-3}$ $U=10 \text{ ms}^{-1}$. For $\frac{\rho_f}{\rho_s} \ll 1$, the frequency should be close to vacuum and then it scales with mass in accordance with Eqn (4.3). Note however the wall effect scales proportional implicating a force coupling which lowers the frequency.

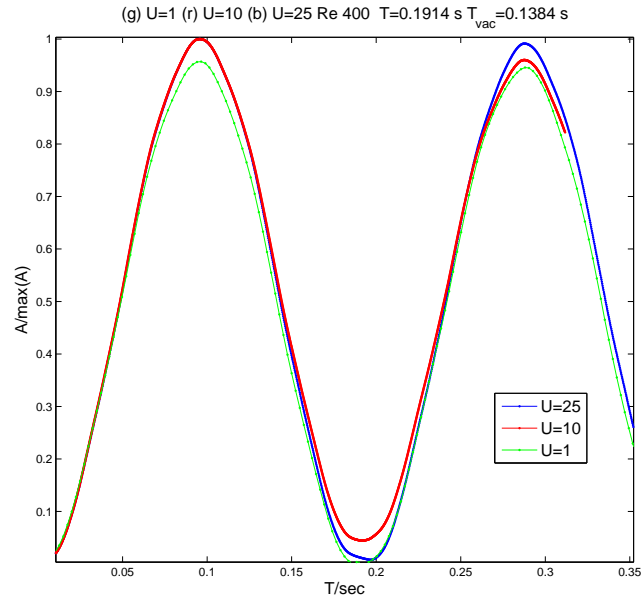


Figure 5.6: The magnitude amplitude of marker point placed at center of the tip. The independence on U for same relative mass for given frequency. $\rho_s = 10 \text{ kgm}^{-3}$, $\rho_f = 1 \text{ kgm}^{-3}$. This is since for same Re the flow pattern is the same, and hence with the same force profile over the structure the same frequency but with a different amplitude will be observed.

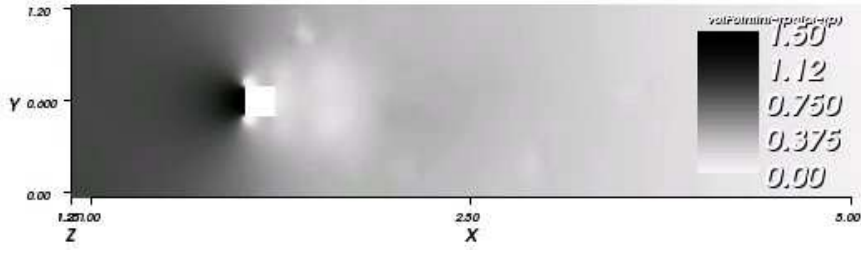


Figure 5.7: The pressure field (p) in XY for $U=1 \text{ ms}^{-1}$ and $Z=1 \text{ m}$, $\rho_s=300 \text{ kgm}^{-3}$, $\rho_f=100 \text{ kgm}^{-3}$ and $Re=400$.

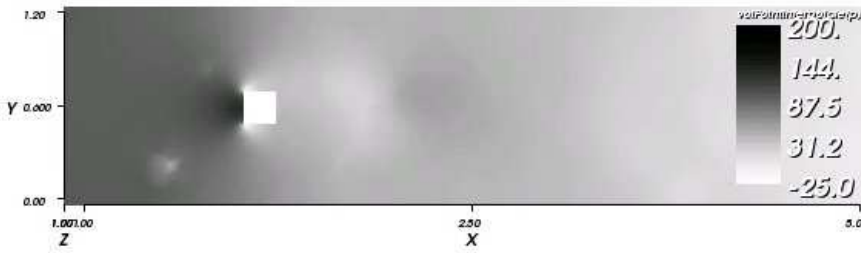


Figure 5.8: The pressure field (p) in XY for $U=10 \text{ ms}^{-1}$ and $Z=1 \text{ m}$, $\rho_s=10 \text{ kgm}^{-3}$, $\rho_f=1 \text{ kgm}^{-3}$ and $Re=400$.

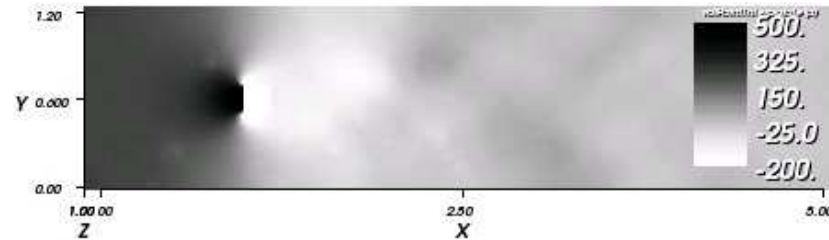


Figure 5.9: The pressure field (p) in XY for $U=25 \text{ ms}^{-1}$ and $Z=1 \text{ m}$, $\rho_s=10 \text{ kgm}^{-3}$, $\rho_f=0.1 \text{ kgm}^{-3}$ and $Re=400$.

The pressure in Figure 5.7-5.9 follows closely Bernoulli's Eqn (4.7). The size of the wake is a function of the Re , the form of the bluff body as implicated by Eqn (2.12). For the same Re and shape of bluff body one can hence expect the same wake size. However different deformed configurations implicates interaction between vortices which change the size of the wake as a result. The free end of the cantilever shape the wake and expects to increase the frequency f_n with increasing amplitude while the confined wall decreases [40]. Further, the pressure on respective side is nearly constant over the whole surface except at the corners, as Figures 5.13-5.15 show. This again support the result of Figure 5.6 that is, the frequency is independent of U , however according to Figure 5.4 the amplitude play a role, but as long as the deviation is small, this doesn't change the wake.

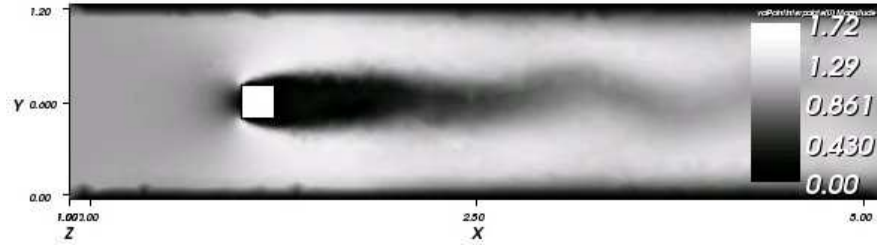


Figure 5.10: The magnitude of velocity ($\|U\|$) in XY for inlet $U=1 \text{ m s}^{-1}$ and $Z=1 \text{ m}$, $\rho_s=300 \text{ kg m}^{-3}$, $\rho_f=100 \text{ kg m}^{-3}$ and $\text{Re}=400$.

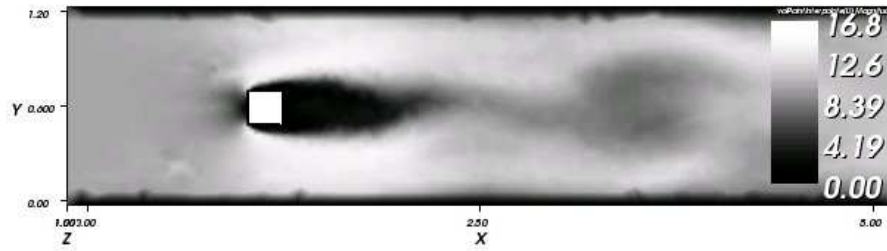


Figure 5.11: The magnitude of velocity ($\|U\|$) in XY for inlet $U=10 \text{ m s}^{-1}$ and $Z=1 \text{ m}$, $\rho_s=10 \text{ kg m}^{-3}$, $\rho_f=1 \text{ kg m}^{-3}$ and $\text{Re}=400$.

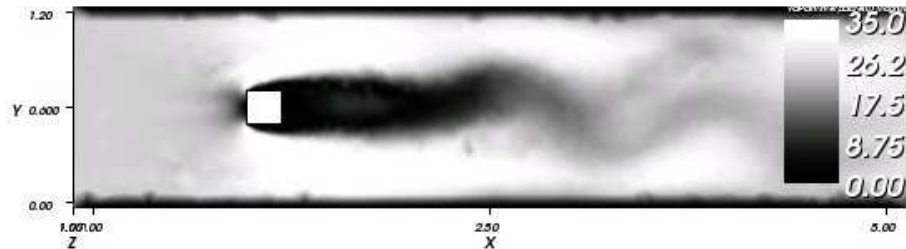


Figure 5.12: The magnitude of velocity ($\|U\|$) in XY for inlet $U=25 \text{ m s}^{-1}$ and $Z=1 \text{ m}$, $\rho_s=10 \text{ kg m}^{-3}$, $\rho_f=0.1 \text{ kg m}^{-3}$ and $\text{Re}=400$.

Figures 5.10-5.12 are the corresponding velocity plots, the increase in speed follows again Eqn (4.7) as expected with pressure drop in corridor adjacent to the cantilever and expected increase in damping due to drag effect. Note the occurrence of areas of possible divergence, which is directly related to the grid structure, see Figure 5.8 and 5.11 and compare it to Figure 4.4 on coordinates (0.6,0.2) and (2.3,2.1) in Figures 5.13-5.18. The sinusoidal shape of the wake gives the frequency of the instability related to the vortex shedding. The size of the wake can be estimated by Figures 5.13-5.18. The tangential line from the tip as demonstrated in Figure 5.17 to cutting the wake size, the low velocity inside the wake is however not a precise measure for the wake. The pressure difference across the structure has its major source in change by the change of the dynamical pressure ($\propto U^2$).

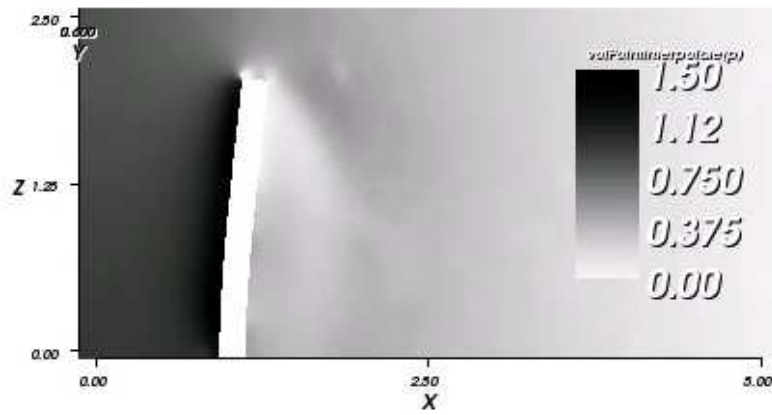


Figure 5.13: The pressure field (p) in XZ for $U=1 \text{ ms}^{-1}$ and $Y=0.6 \text{ m}$, $\rho_s=300 \text{ kgm}^{-3}$, $\rho_f=100 \text{ kgm}^{-3}$ and $Re=400$.

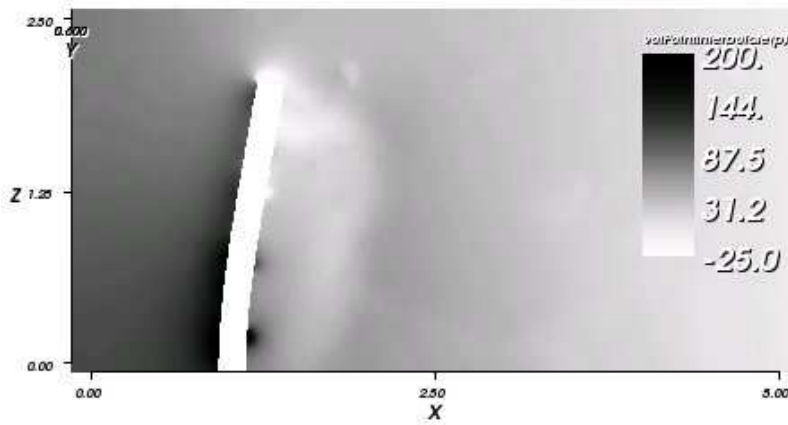


Figure 5.14: The pressure field (p) in XZ for $U=10 \text{ ms}^{-1}$ and $Y=0.6 \text{ m}$, $\rho_s=10 \text{ kgm}^{-3}$, $\rho_f=1 \text{ kgm}^{-3}$ and $Re=400$.

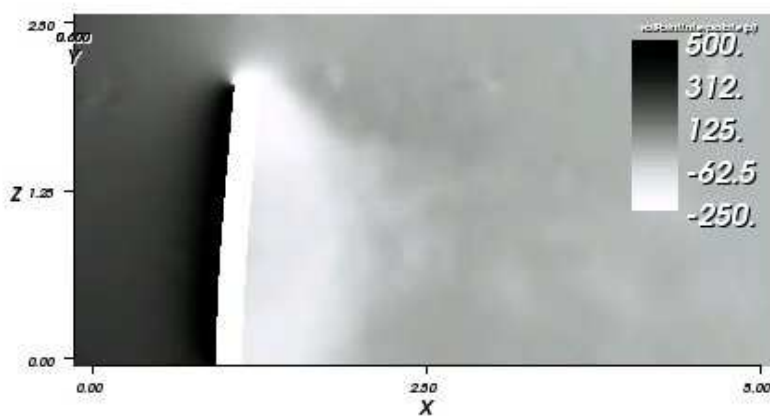


Figure 5.15: The pressure field (p) in XZ for $U=25 \text{ ms}^{-1}$ and $Y=0.6 \text{ m}$, $\rho_s=10 \text{ kgm}^{-3}$, $\rho_f=0.1 \text{ kgm}^{-3}$ and $Re=400$.

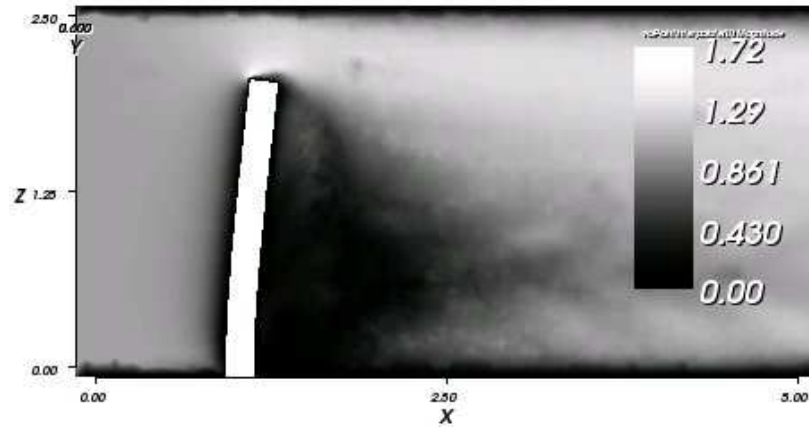


Figure 5.16: The magnitude of velocity ($\|U\|$) in XZ for inlet $U=1 \text{ ms}^{-1}$ and $Y=0.6 \text{ m}$, $\rho_s=300 \text{ kgm}^{-3}$, $\rho_f=100 \text{ kgm}^{-3}$ and $Re=400$.

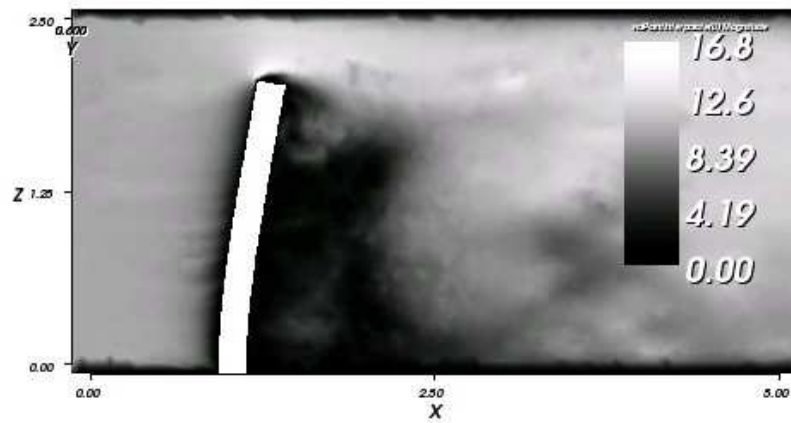


Figure 5.17: The magnitude of velocity ($\|U\|$) in XZ for inlet $U=10 \text{ ms}^{-1}$ and $Y=0.6 \text{ m}$, $\rho_s=10 \text{ kgm}^{-3}$, $\rho_f=1 \text{ kgm}^{-3}$ and $Re=400$.

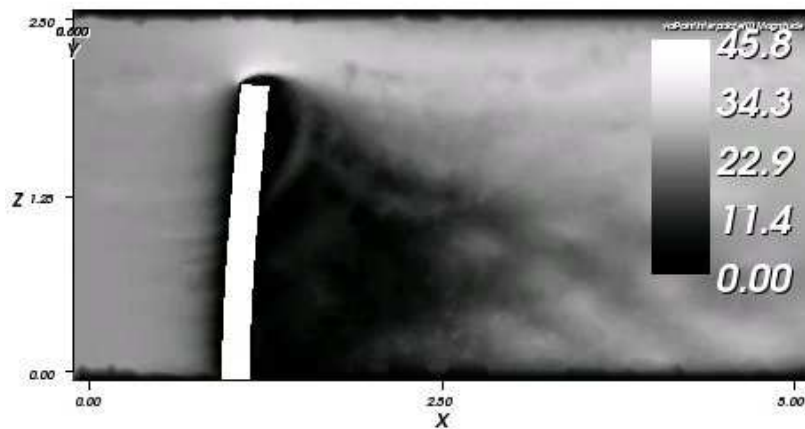


Figure 5.18: The magnitude of velocity ($\|U\|$) in XZ for inlet $U=25 \text{ ms}^{-1}$ and $Y=0.6 \text{ m}$, $\rho_s=10 \text{ kgm}^{-3}$, $\rho_f=0.1 \text{ kgm}^{-3}$ and $Re=400$.

5.5 Error analysis

Error analysis is performed on each domain separately and then an error estimation of the time period is presented.

5.5.1 icoDyMFoam

OpenFOAM provides a post-Processing utility to estimate the error, *icoEstimateError*, a local residual formula presented in the thesis in [28]. By studying the difference between Eqn (2.17) and Eqn (2.19), then discretize to the second order, one obtains a transport equation for the error flux. This utility implicates no instability is caused by the FSI algorithm, since the error flux is the same *before* FSI and *after*. The static error originates mainly from the convective term, by studying the case $U=1 \text{ ms}^{-1}$ and $U=10 \text{ ms}^{-1}$ from Figure 5.19 and Figure 5.20, is increased by a factor of 10. Note however that this utility doesn't estimate the error in the transient part which due to the high Co is of significance. The probes in the fluid revealed high frequency error pulse, with the frequency of the vortex release, which is a result when the vortices enter the zeroGradient outlet boundary condition, hence the pressure correction gives a shift in total energy which is reduced when the transient process by initial movement of the cantilever enters the steady state region. From Figures 5.19-5.21 one obtains that the major source of error lies in the wake, the vortices and at points of interest due to possibility of divergence in the grid, as Figure 4.4, 5.8, 6.3 and 5.11 illustrates. There were three cases which had divergence in the PISO loop, they are connected to the error in the convective term but there are at least four more cases that showed the same tendency, as Figure 5.8 implicates. The PISO in icoDyMFoam within the loop doesn't correct for the orthogonality, since it has been observed to cause instability in convergence. This is done as a last correction [28]. Figure 5.15 show the connection between the failed convergence point and the estimated error at the divergence points in pressure field in the wake, note the lowest level since that point is the common factor in all diverged cases. The relevant question mark for Figure 5.16-5.18 is the origin of this regular error at the cantilever at three different heights. An analysis of the axial mode of frequency, indicates a relation to the release of the axial modes of vorticity.

5.5.2 DynamicElastic

FFT analysis on the marker points for analysis revealed that unknown high frequencies with an amplitude strength relative to the natural frequency of order of 1:1000, only notable in Z direction, with no correlation to ρ_f and varies linearly with the ρ_s . The frequencies of question are $58 \pm 2 \text{ Hz}$, $73 \pm 2 \text{ Hz}$ and $178 \pm 2 \text{ Hz}$. This implicates the possibility that excited axial modes appear. The Crank-Nicholson error caused by staggered technique in state space creates an error with high frequency error, and from the verification of DynamicElastic showed no such feature. This favor the interpretation that the observed frequencies are excitations from the variation of pressure due to the vorticity acting on the tip of the cantilever and since the large difference in frequency between fluid and natural frequency for the solid, the mode seen in the marker point is the natural frequency for longitudinal mode. The error from the probes with the signal noise caused by the vortices is a constant shift, this doesn't affect the solid state since its movement is built upon the pressure difference, hence canceling out the noise.

5.5.3 Estimated Error in the period

By taking the sum of the relative error to the contributing Eqn (4.3), the total estimated error ΔE for T_c is the sum of the modeling error of solid ($T_n = \frac{1}{f_n}$), estimated by table 5.1, the force term in fluid $\propto U^2$ (U) estimated by Figure 5.19-5.21 from the same cases presented in section 5.4.3 and the measurement error (T_c) from table 5.3,

$$\Delta E = \frac{\Delta U}{U} + \frac{\Delta T_n}{T_n} + \frac{\Delta T_c}{T_c}. \quad (5.2)$$

This gives a relative error of the order 5-25%, where on average 3% error arise from the U, the T_n have an error around 2% while the measured time period lies between 5 – 20%. The degree of influence of the wall on Dev is a relevant issue but the present error bars are too large to actually answer this question. The major source of error is that the simulation is limited in time, only partial periods evolved, and the transient effect as seen by Figure 5.2. The number of periods required is not that cannot be estimated, it's something that will be revealed during the simulation. The study indicates although a smaller error due to the following observations,

- All shift by Eqn (2.62) have the correct sign.
- The scaling effects in parameters are precise, Figure 5.5.
- The amplitude formula Eqn (2.63) show less average error.
- The optimization Eqn (5.1) implicates a systematic shift.

It is therefore a system dependent error that is relative and proportional to the quantity observed, hence implicating either an error in the mesh or it's related to the boundary condition of inlet or the wall effect [40]. The time period is not likely affected by the poor resolution of the Karman effect, the frequency depends on the dynamics of deflection of the fluid around the object, an area that has a good grid resolution, which is the above error estimate for the fluid taken from the Figures 5.19-5.21. The error is mainly generated by the wake and from plots the axial modes of release on vortices is clearly seen, due to the interaction with the free end one can see a partial mode A with nodal plane at the midpoint of the cantilever in Figure 5.22 and 5.24. Figure 5.23 is beginning to diverge and this pattern with regular error points on the surface is a peculiar feature in divergence in the pressure correction. The divergence is often a slow process, it gradually increases the pressure until a point where pressure correction fails. Due to CD there is divergence originating from non-orthogonal cells note especially the point in XY plane at (0.6,0.2) and compare it to Figure 4.4.

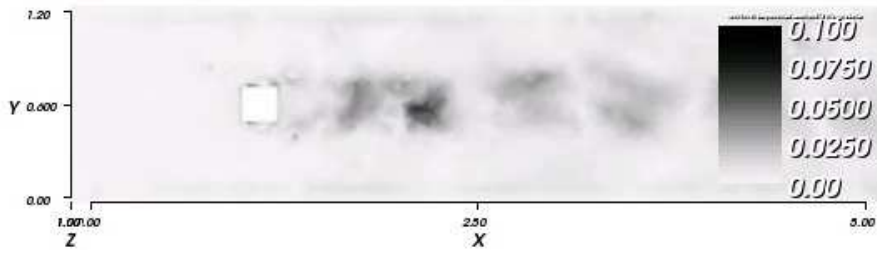


Figure 5.19: The estimated velocity error in XY for $U=1 \text{ ms}^{-1}$ and $Z=1 \text{ m}$, $\rho_s=300 \text{ kgm}^{-3}$, $\rho_f=100 \text{ kgm}^{-3}$ and $Re=400$.

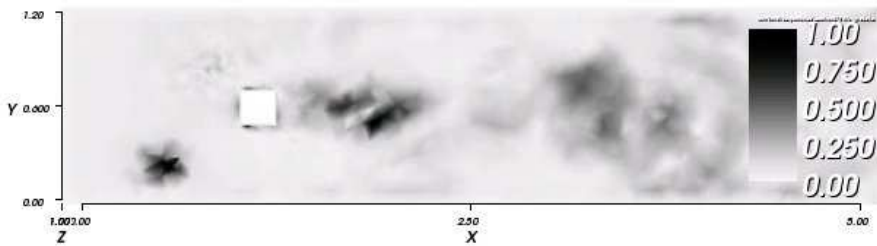


Figure 5.20: The estimated velocity error in XY for $U=10 \text{ ms}^{-1}$ and $Z=1 \text{ m}$, $\rho_s=10 \text{ kgm}^{-3}$, $\rho_f=1 \text{ kgm}^{-3}$ and $Re=400$.

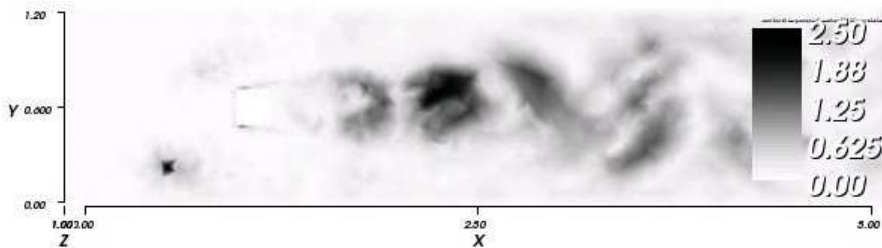


Figure 5.21: The estimated velocity error in XY for $U=25 \text{ ms}^{-1}$ and $Z=1 \text{ m}$, $\rho_s=10 \text{ kgm}^{-3}$, $\rho_f=0.1 \text{ kgm}^{-3}$ and $Re=400$.

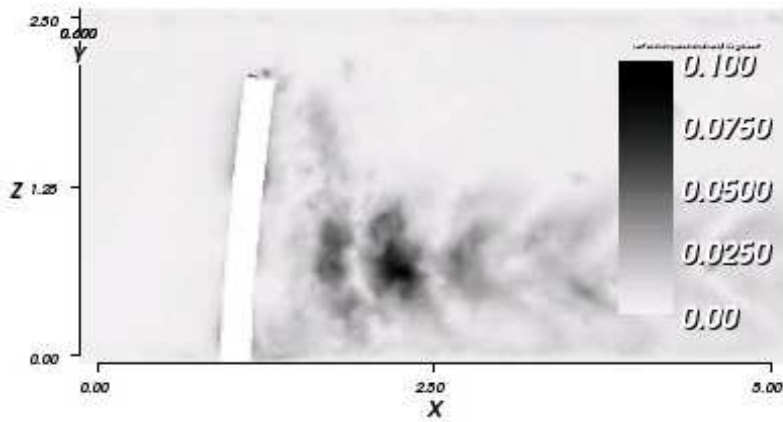


Figure 5.22: The estimated velocity error in XZ for $U=1 \text{ ms}^{-1}$ and $Y=0.6 \text{ m}$, $\rho_s=300 \text{ kgm}^{-3}$, $\rho_f=100 \text{ kgm}^{-3}$ and $Re=400$.

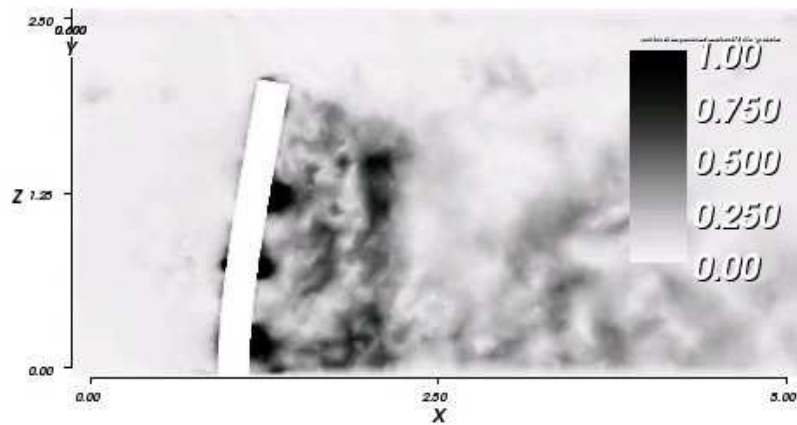


Figure 5.23: The estimated velocity error in XZ for $U=10 \text{ ms}^{-1}$ and $Y=0.6 \text{ m}$, $\rho_s=10 \text{ kgm}^{-3}$, $\rho_f=1 \text{ kgm}^{-3}$ and $Re=400$.

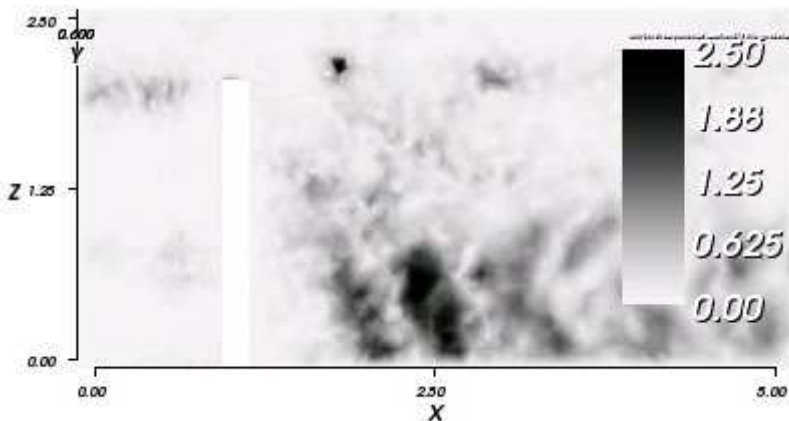


Figure 5.24: The estimated velocity error in XZ for $U=25 \text{ ms}^{-1}$ and $Y=0.6 \text{ m}$, $\rho_s=10 \text{ kgm}^{-3}$, $\rho_f=0.1 \text{ kgm}^{-3}$ and $Re=400$.

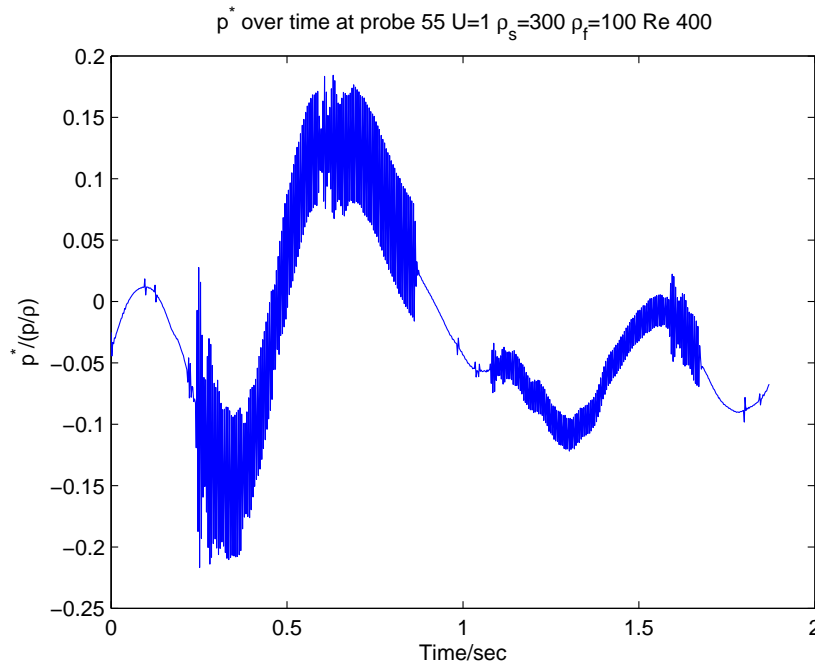


Figure 5.25: Probe 55 in the fluid in $U=1 \text{ ms}^{-1}$. This plot comes from the VIV study in the next chapter, the in-line motion is damped which could explain the lowering in size of the white noise in Figure 5.25. The reason for this behavior is that when the vortex enters outlet, due to the zeroGradient patch on outlet for velocity, it introduces an error which is showed as noise as long it passes over the gradient. The whole spectra of error in the probes was not fully studied due to limited time for the project.

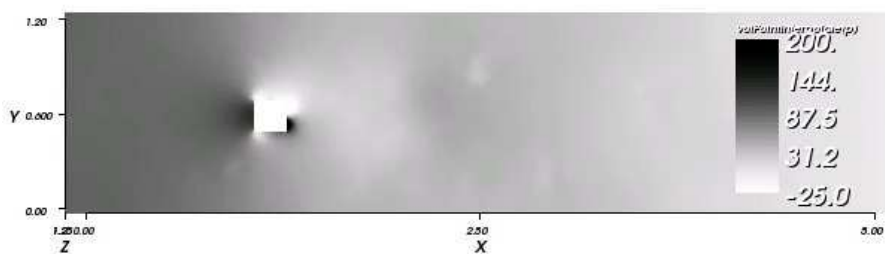


Figure 5.26: The divergence at $U=10 \text{ ms}^{-1}$ in XY at $Z=1.25 \text{ m}$, $\rho_s=10 \text{ kgm}^{-3}$, $\rho_f=1 \text{ kgm}^{-3}$ and $Re=400$. Several cases provide an error as exemplified in Figure 5.14, which this figure illustrates close with a XY cut at $Z=1.25 \text{ m}$. Exact same type of divergence was observed while using semi-discretization with $\theta = \frac{1}{2}$ for the fluid a study omitted in this report. This is well documented within the OpenFOAM community over the classical oscillation in using CD together with Crank-Nicholson.

5.6 General comments

A brief discussion on the blending in time semi-discretization, the difference between explicit and implicit FSI followed by an analysis of the used acceleration techniques.

5.6.1 The theta method

The theta method gives explicit, implicit and Crank-Nicholson semi-discretization of the time variable. The damping introduced by implicit Euler ($\theta = 1$) compared to Crank-Nicholson ($\theta = \frac{1}{2}$) is notably larger as showed by Figure 5.27. As indicated during the verification of the *DynamicElastic*, $\theta = \frac{1}{2}$ is energy conservative. The damping observed for $\theta = \frac{1}{2}$ in Figure 5.27 comes from the implicit temporal discretization in the fluid and the drag effect. The explicit Euler method $\theta = 0$ failed due to the induced counter pressure originating from the Bernouillis relation ($\Delta P = -\rho_f \frac{1}{2} v^2$), that is when velocity v of the adjacent fluid cell to structure changes, a pressure change ΔP will be introduced with opposite sign as a function of the speed v of the structure. As a rough estimate, when the v approaches the same velocity as the inlet, the explicit solver will diverge. This implicitly set the upper limit for displacement taken to be $U \cdot \delta t$ which in turn limit the time step. However, the inertia of the solid structure stabilizes the system, the above relation is for $\rho_s \leq \rho_f$, higher stability is achieved by $\rho_s > \rho_f$.

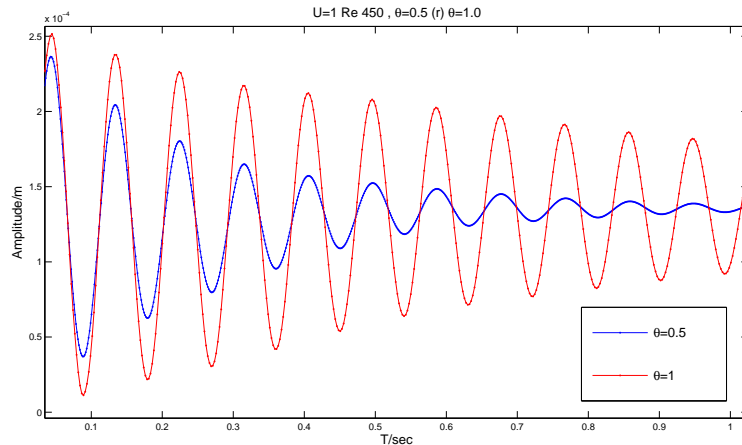


Figure 5.27: The Implicit semi-discretization in time ($\theta = 1$) compared to Crank-Nicholson ($\theta = \frac{1}{2}$) for $U=1 \text{ m s}^{-1}$, $\rho_s = 10 \text{ kg m}^{-3}$ and $\rho_f = 1 \text{ kg m}^{-3}$ with $\text{Re}=400$. The significance of the damping of the fluid is illustrated since with the current mesh for the structure the damping in the structure is insignificant.

5.6.2 Explicit/Implicit FSI

The FSI implemented offers explicit and implicit coupling solution, also known as weak and strong coupling. Test calculations have shown that with damping there is no significant difference between the methods using the settings from section 5.4.1, the same convergence pattern. The explicit case with $\rho_s \leq \rho_f$ shows same divergence for same reason as the explicit time step in the semi-discretization in section 5.6.1. The gain in using implicit coupling is

together with ROM step gaining an accuracy of several order and a gain in computational speed is expected if the tolerance could be chosen adaptively.

5.6.3 Aitkens relaxation and the ROM

For $\frac{\rho_f}{\rho_s} > 1$ and for flexible structures, the Aitkens relaxation method is of significant importance, where a gain in speed of convergence by a factor 4 is observed or even more. These reproduce the values of iterations reported elsewhere [53, 33], although higher order errors will be introduced for non-linear functions due to the interpolations, indicating the favor for ROM techniques. As indicated from [33] where a diagram shows that not until higher tolerances than $1 \cdot 10^{-6}$ a gain was obtained in iterations in the sub-cycle step by using ROM, but due to the nature of this problem, there was little need for having higher precision unless studying higher frequencies. The Aitkens relaxation normally converged within 2-7 iterations, exceptions occurred whenever $\omega_n \rightarrow 0$ resulting in a drift with an increased error on average 20-30 times the tolerance, with an error of the order 10^{-5} in present study, negligible for all practical consideration. In applying the 3-ROM with its FD formula gave no

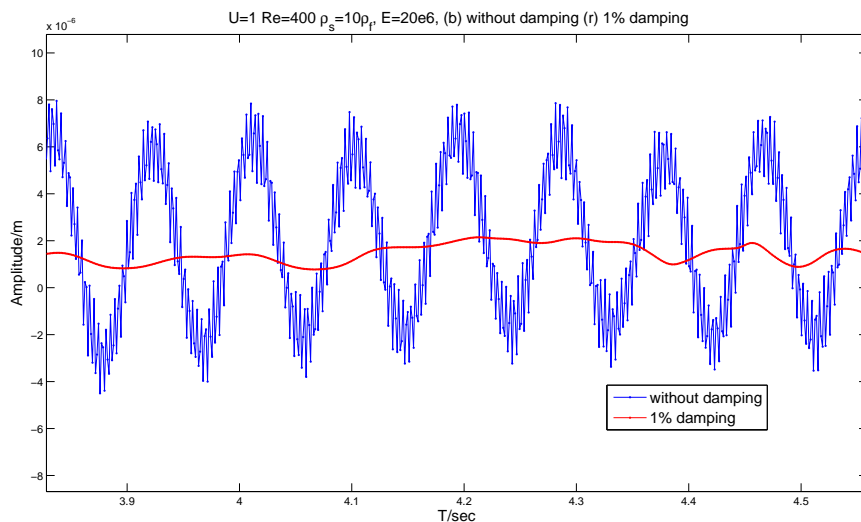


Figure 5.28: Marker at the cantilever center point on the tip (X component). The regular pattern appearing as noise, is the high frequency from the longitudinal waves in the cantilever (Z-component) and the effect of damping at 1%.

gain in computational speed between time steps due to its inherited divergence property with a scaling factor of 3. By taking the test function e^x it can be demonstrated that the current 3-ROM worked excellent as long as the interpolation step was *exactly* known, however, due to the coupling term, the dynamics change the interpolation and introduces an error and this made the interpolation collapse since the deviation was increasing creating a counter pressure effect which made the solution crash within a few cycles. Similar behavior as to explicit semi-discretization except for three simulation followed by one ROM step. The origin to the disastrous result with 3-ROM is related to the Courant number and the introduced signal to noise ratio, see Figure 5.28, a small error in the displacement introduce error in the fluid solver. In other words the FD strategy is not a good choice as interpolation technique. The reason why the sub-cycle iteration don't diverge is that Aitkens relaxation auto correct

the error and at the convergence point for the given threshold in a sub-cycle, a significant improved accuracy is gained during the up to two orders since the formula for FD works well when the coupling effect can be *ignored* between the fluid and the solid. By introducing damping the performance can be improved between the time steps making the error decay during the normal FSI cycles. However, a proper analysis is required to not deteriorate the physics, as Figure 5.28 illustrates with over-damping. An improved ROM technique involves either a Proper-Orthogonal-Decomposition technique (POD) [16] or a residual method as Gauss Newton [54].

5.7 Multiple block case

The multi-cantilever case from section 4.5 was chosen in this study using section 4.7 and 4.3. The main purpose of this study is to reproduce the frequency of the single cantilever with four cantilever case. However, a complicated issue with the laplacian schemes for the pseudo-displacement scheme and their pressure correction causes divergences in some of the cases. But all the converged result shows, that the cantilever is moving towards each other as to be expected by theory. The lines with larger amplitudes in Figure 5.29 are the two front

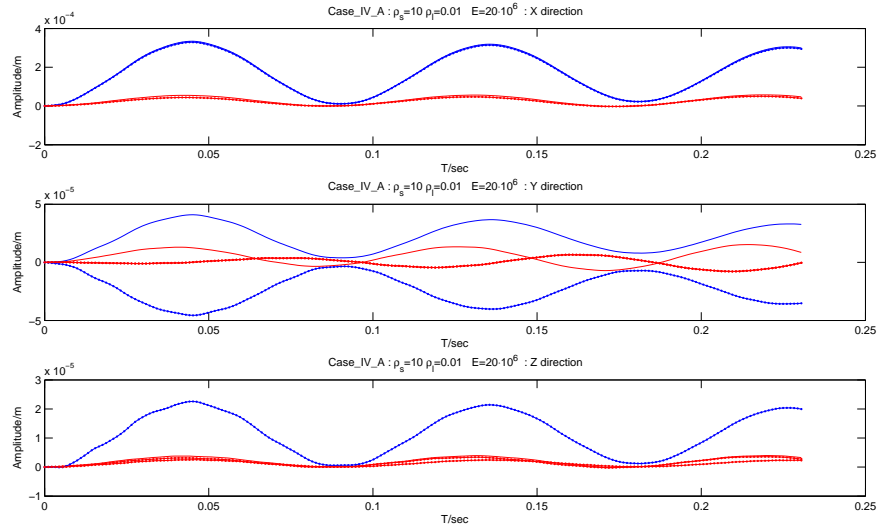


Figure 5.29: The marker point coordinates for $U=1 \text{ m s}^{-1}$, $\rho_s = 10 \text{ kg m}^{-3}$, $\rho_f = 0.01 \text{ kg m}^{-3}$ and $Re=400$. Front cantilevers are with larger amplitude and those behind in the wake have smaller.

cantilever and those lines with smaller amplitude are the cantilevers behind, indicates less deformation for the cantilever in the wake of the front, and all four even phase shifted have the same time period, comparable to the one cantilever case, $T_c=0.0768 \text{ s}$ for $U=1 \text{ m s}^{-1}$ and $T_c=0.1053 \text{ s}$ at $U=10 \text{ m s}^{-1}$. Eight more cases had slow convergence, such that not even a half period evolved. The convergence increases linearly with the number of cantilevers, the Aitkens relaxation converges within 5-20 iterations on average. In total one third of all calculations diverged.

5.8 Conclusion

The FSI reproduces the frequency shift well within the margin of error of the mesh quality and the measurement of the time period. The amplitude correlation study, the scaling and the independence of velocity in the frequency increases the confidence that the FSI algorithm works as intended. The error analysis from section 5.5.1 is incomplete since it lack an estimate of the transient effect and not study the refinement effect to confirm the convergence in parameters is achieved. However, the error lies as expected within the wake, the vortices and areas of possible divergence in the grid and it increases linearly with the flow speed. Figure 5.25 implicates the presence of transient error which is decaying and hence the dynamical path in momentum space could not be reliable but the pressure change is more and less a constant shift and don't affect the pressure *difference*. The CD is used in the numerical boundary conditions and the zeroGradient flux BC is the source of the discretization error [28]. Although the method is stable an issue appear while using two sequential solvers, see Figure 5.30. The dilemma arise due to that the solid is more accurate and stable than the fluid. Therefore, the upper bound for the time step is given by the fluid solver. However, due to a combination between temporal discretization and the transfer step where viscous traction is determined by displacement field which where the interpolation formula have higher error than the solid solver, a lower bound is obtained from the solid. This implies that the total algorithm, seldom achieve the individual solvers optimal performance and there will be situations that for given tolerance, there is no convergence although each individual converges.

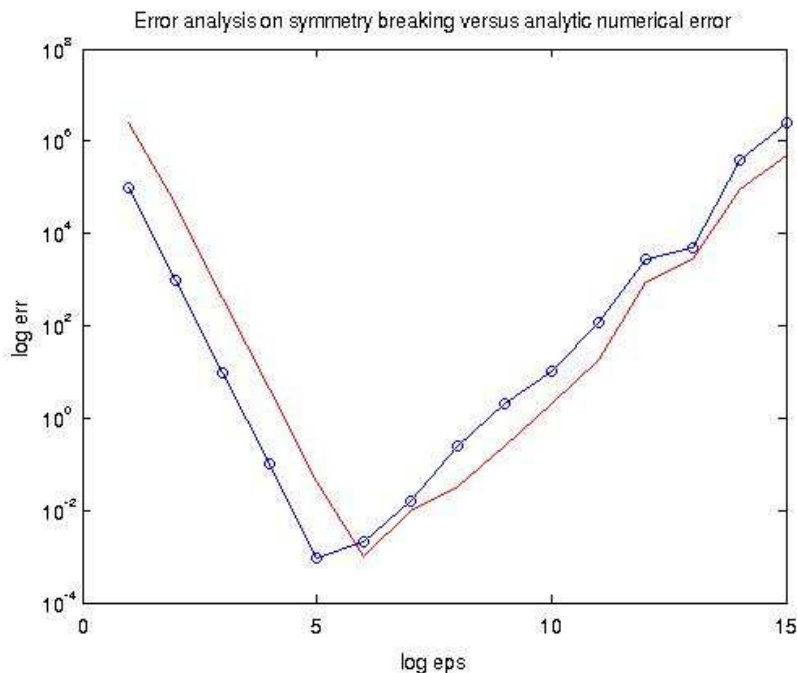


Figure 5.30: The numerical precision entering the point of floating error. The characteristic upper and lower limit in grid size for a given tolerance. Taken from the course assignment 1 in FMN110 (2007). [14]

Chapter 6

An application to VIV

The lock-in frequency of the fluid driven motion on the structure is studied in this chapter. By using probes on the structure and in the fluid the coherent movement is verified by FFT and the result is compared to the experimental fluid frequency to given Reynolds number. Eqn (4.4) implicates over 90% of the strain energy in the validation steps originates from the in-line motion and therefore an artificial damping must be used to unmask the VIV components.

6.1 Problem description

The dimensionless parameter Strouhal number (St) relates to the frequency of the vortex release caused by the deflection of the streamlines around the immersed body. The larger the body the smaller the frequency, the larger velocity the higher the frequency. The characteristic St for VIV was observed experimentally to be [68],

$$St = \frac{fl}{U} = 0.198\left(1 - \frac{19.7}{Re}\right). \quad (6.1)$$

The vorticity can be identified by the term $\nabla \times \mathbf{U}$ in Eqn (4.5), which describes the rotation of the fluid, giving cause to the Karman vortex street Figure (1.1). In a simplified form, it can be expressed as the energy that cost to divert the flow is the energetic content in the vortex and hence the induced strength in the transversal force. The St depends on the velocity (U) and the characteristic length (l) of the body. The vortex has a three dimensional structure, and is released from the cantilever periodically along the centerline in modes A and B discussed in [21] implying that any point behind the cantilever in the domain of dependence can be representative to evaluate the St , from the variation of the pressure. The classical description of the modes 2S,2P and so forth is obtained from experiments using thin layer flow (2D), however, the mid point of the cantilever due to the nodes of A and B gives the same two dimensional flow pattern.

6.2 Setup

For the settings of the case, the section 4.3, 4.4 and 4.7 is used. The in-line driven flow motion of the cantilever is nearly decoupled from the vortices released from the sides of the cantilever. For this reason the FFT spectra in Y direction gives the VIV frequencies. Table 5.3 requires the correct case to be chosen such that at least 5 vortices released during simulation

to estimate the frequency for the cases which revealed the VIV due to the damping in given time window, that is an amplitude of order $1 \cdot 10^{-2}$ m. For this reason, the following cases were chosen, $U=1, 10$ and 25 ms^{-1} with ρ_s as 300, 10 and 10 kgm^{-3} respectively ρ_f as 100, 1 and 0.1 kgm^{-3} . One particular feature of simulations from section 5.4.3 is the dominance in the in-line driven motion, the actual VIV is of an factor 100 or less in displacement length from starting position. By using the moderate damping such that the VIV becomes more dominant since energy is continuously introduced by the energy content of the vortex. It is at this point clear that without damping in fluid or structure, the amplitude will have negative damping. The calculations were therefore performed with 0.1% damping such that the in-line driven motion is drained and transversal motion remains. The observed frequencies in the cantilever are those of the marker probe placed at the center of the tip of the free end. These are compared to the averaged spectra of Fourier analysis for the 120 probes in the fluid aligned from six lines in X direction, from middle height and top cantilevers free end, 3 lines at each level, taking the middle point and corners of the surface, 20 points starting with 0.2 m distance from the cantilever and 0.2 m between each point. The Fourier analysis is performed as far as possible the accuracy allows from the transient part of the spectra.

6.3 Result

The study have its origin from the case $\rho_s = 10 \text{ kgm}^{-3}$ and $\rho_f = 0.1 \text{ kgm}^{-3}$ at $U=1 \text{ ms}^{-1}$, Figure 6.1 from which no significant exchange in energy between fluid and solid, show a particular wave packet in Y direction, which revealed the VIV for the first time in this project. There is no observed damping in the system since fluid is in steady state flow with no significant exchange, its a perturbational response to the forces and the cantilever is loading up the frequency and damped in time by the inherited energy loss in the discretization. There will be a damping observed in the marker point data if the coupling term with the fluid is removed. The probes data in the fluid data contained a white noise signal in period, see Figure 5.25. This is with a frequency similar to the release of vortices, which itself is not a problem since INS is independent of absolute data and the FSI is driven by the pressure difference over the cantilever. However a question arise of the significance of the effect in FSI as when structure enclose the fluid like flow in a pipe, then the response is based on absolute data. The FFT analysis on marker point in solid for $U=1 \text{ ms}^{-1}$ gives a VIV time period of 1.45 s (0.69 Hz) as seen from Figure 6.9 red line (Y) while the blue line (X) is masked by the in-line movement. As the frequency of VIV can be read either from the white noise signal mentioned above and in section 5.5.3 it can be compared to the average FFT spectrum of the fluid probes given by Figure 6.11 to be around 1-0.7 s (1-1.3 Hz). The FFT spectra for the solid Figure 6.13 with $U=10 \text{ ms}^{-1}$ gives around 0.16 s (8 Hz) time period in the solid and for the probes in the fluid Figure 6.14, which is estimated to be around 0.07-0.14 s (7-14 Hz). From Figure 6.16 the FFT spectra $U=25 \text{ ms}^{-1}$ case give VIV at 0.064 s (15 Hz) and the averaged fluid probes FFT analysis gives a value around 0.04-0.06 s (17-25 Hz), Figure 6.17. As clearly seen from the Figures 6.11-6.17, the uncertainty is relatively high for the fluid probes. By the Eqn (6.1) one can conclude the frequency should be 1 s (1Hz), 0.1 s (10Hz) resp 0.04 s (25Hz). However the validity of the formula is somewhat questionable, the confining walls and the shape of the bluff object have influence as well as the free end of the cantilever. Out of the previous 23 simulations it was observed that 12 simulations were observed with VIV. The analysis of these is complicated by not using damping in these cases hence the amplitudes have relative large range of error. The time period is supposed to increase due to the mixing of the wakes [40] but also the free tip wake mechanism will introduce a shredding of different frequency [31]. It was also observed multiples of frequency

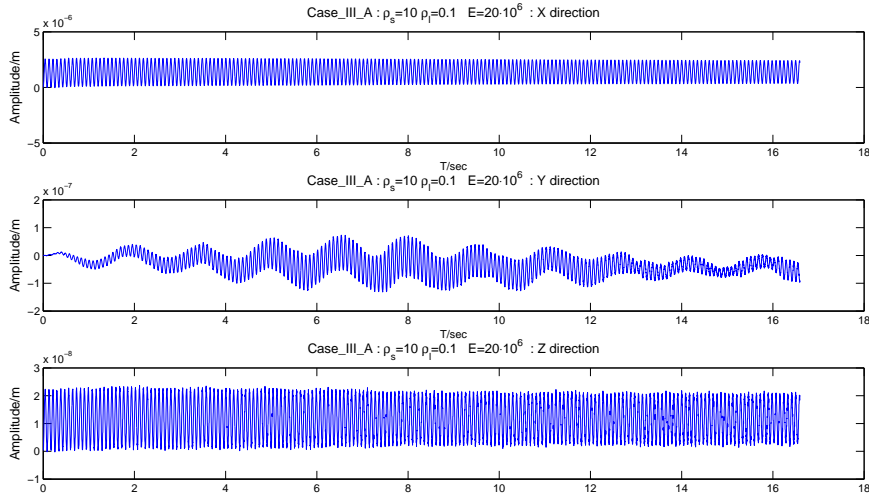


Figure 6.1: A marker point spectrum from validation step, $U=1 \text{ ms}^{-1}$, $\rho_s=10 \text{ kgm}^{-3}$, $\rho_f=0.1 \text{ kgm}^{-3}$ and $\text{Re}=400$, with X,Y,Z components over time from top and down. Although the result is non-physical due to out of range of continuum, it had numerical the purpose to prove the stability and that the natural frequency was correct. Note however the Y component (middle figure) contains a wave-packet where the lower frequency is the VIV frequency and higher frequency the natural frequency.

of VIV, most clearly seen in Figure 6.16 and the origin for this lies partly in the failure of exactly representing a sinusoidal movement and the instability of the wake, that gives higher order terms in the spectra as multiples of the lower. Using the 12 cases with VIV with the difficulty in finding a measurable A_y component show that the study had 7 unique points that could be used for a plot of reduced velocity versus the reduced amplitude and the quotient $\frac{f_n}{f}$ [58]. The reduced velocity plots in Figure 6.8 reproduces the linear dependency while the amplitude response cannot be relied on due to the wall effect, apart from one thing, the point of reduced velocity where the stationary flow induce an unsteady motion. The plot of V_r versus $\frac{f_n}{f}$ show a linear dependency, but since no true lock-in frequency case been studied, that is $f = f_n$, the flattening of the curve is absent in this study [58]. One interesting point is the difference between the XY and the XZ plane, the impression is given that the *size* of vortices decreases linearly by time in the XZ plane. This is a false picture, the purpose for showing these figures is to show the importance of the vortices released from the tip.

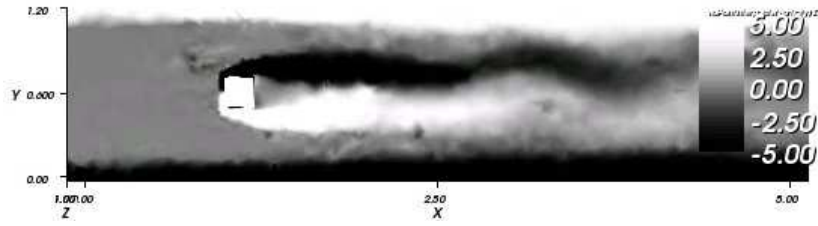


Figure 6.2: $\partial_x U_y - \partial_y U_x$ in XY for $U=1 \text{ ms}^{-1}$ and $Z=1 \text{ m}$, $\rho_s=300 \text{ kgm}^{-3}$, $\rho_f=100 \text{ kgm}^{-3}$ and $Re=400$.

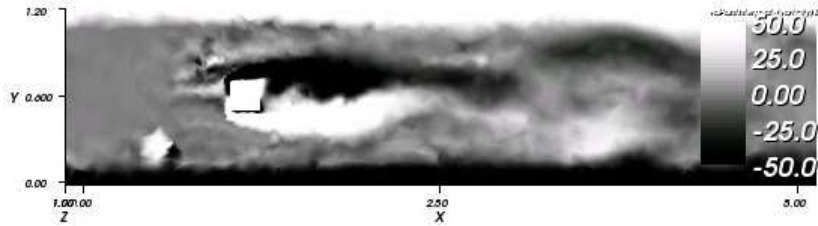


Figure 6.3: $\partial_x U_y - \partial_y U_x$ in XY for $U=10 \text{ ms}^{-1}$ and $Z=1 \text{ m}$, $\rho_s=10 \text{ kgm}^{-3}$, $\rho_f=1 \text{ kgm}^{-3}$ and $Re=400$.

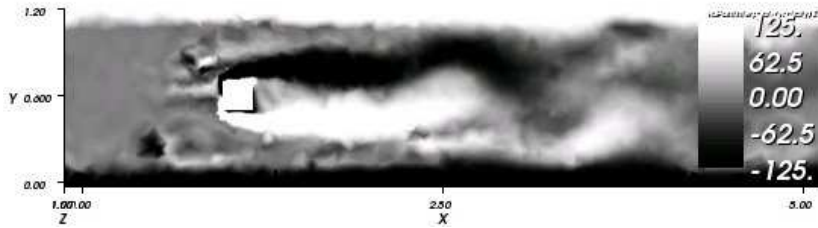


Figure 6.4: $\partial_x U_y - \partial_y U_x$ in XY for $U=25 \text{ ms}^{-1}$ and $Z=1 \text{ m}$, $\rho_s=10 \text{ kgm}^{-3}$, $\rho_f=0.1 \text{ kgm}^{-3}$ and $Re=400$.

From Figures 6.2-6.4 the Z-component of the vortex show the alternative spin in going from the wall to the closest point of release on the cantilever and the opposite spin over the structure and thus shaping the wake. From this it is clear that the wall will give the impression of stable vortex release. The release is unstable meaning increasing size of the vortex without the walls in time [68]. The tip have strong vortices release and affects the wake size as a function of the deflection. Figures 6.2-6.4 show same size of wake due to Re , however Figure 6.3 is smaller as expected due to the free tip for cases with larger amplitudes. Figures 6.5-6.7 show the influence of the free end tip of release of vortices, tangential to the surface, however only an animation gives the dynamics clear picture that the vortices going from the tip are tangential from the surface of the tip.

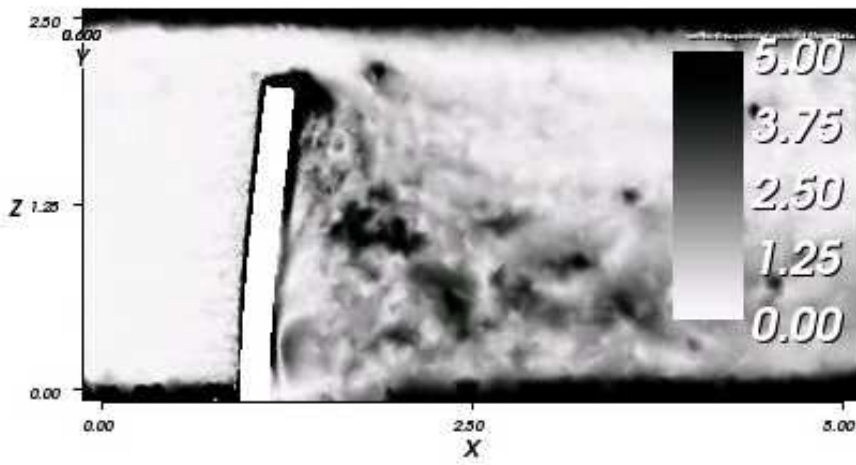


Figure 6.5: total vorticity in XZ for $Y=0.6$ m at $U=1$ ms^{-1} , $\rho_s=300$ kgm^{-3} , $\rho_f=100$ kgm^{-3} and $Re=400$.

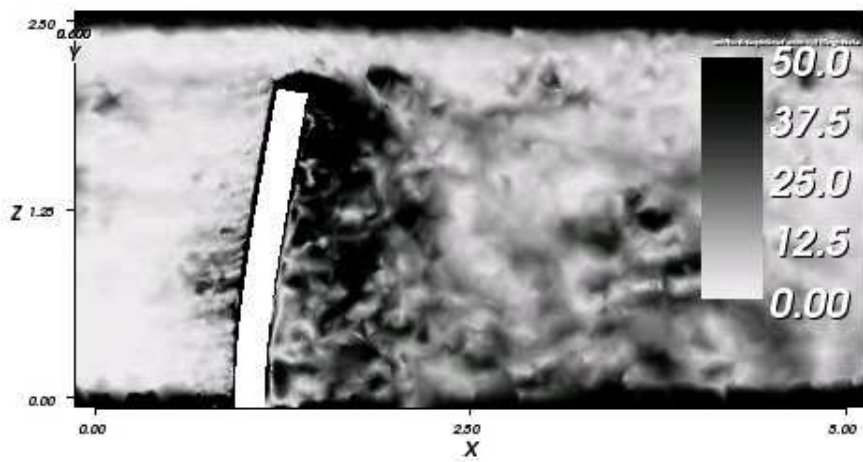


Figure 6.6: total vorticity in XZ for $Y=0.6$ m at $U=10$ ms^{-1} , $\rho_s=10$ kgm^{-3} , $\rho_f=1$ kgm^{-3} and $Re=400$.

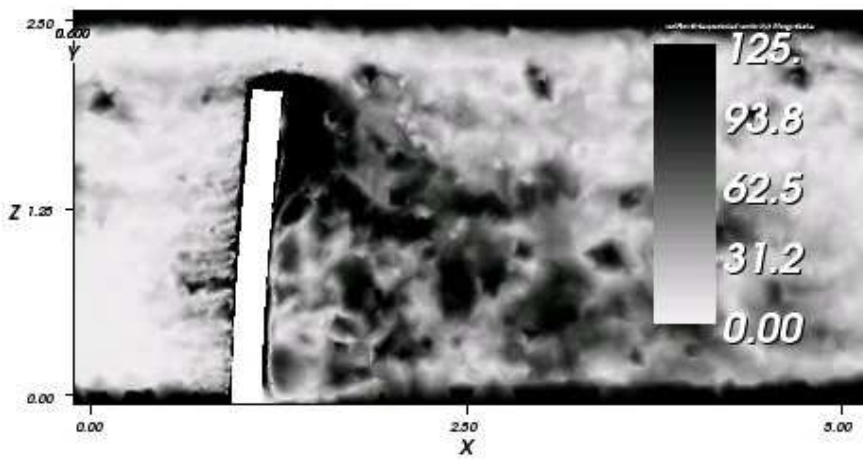


Figure 6.7: total vorticity in XZ for $Y=0.6$ m at $U=25$ ms^{-1} , $\rho_s=10$ kgm^{-3} , $\rho_f=0.1$ kgm^{-3} and $Re=400$.

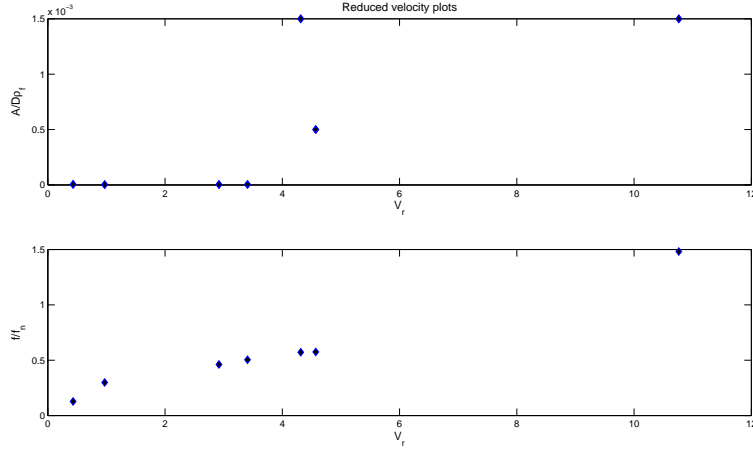


Figure 6.8: Reduced velocity $V_r(\frac{U}{f_n D})$ plots, The lower figure is V_r v.s. $\frac{f}{f_n}$ and upper V_r v.s. $\frac{A}{\rho}$. The figure reproduce the linearity of the lower and the initial branch for the upper, i.e. the region where the VIV enter resonance with the structure.

The reduced velocity plots cannot due to the wall effect which stabilize the vortices, reproduce the data for the amplitude response, since it is related to a switch between 2S and 2P mode which is not plausible due to the confined wall, but it is expected to give the linearity in the reduced velocity and the reduced frequency since this is independent to the mode. However, the point at which strong interaction is predicted to occur seem to be indicated in Figure 6.8. Since the data was insufficient for a proper plot, the Eqn (4.8) was used for a fluid with density equal to one, the amplitude was hence divided by fluids density. From Table 6.1 one can see the correct scaling in frequency due to Eqn (6.1), however, in

Inlet velocity (U/ms^{-1})	Fluid frequency (f/Hz)
1	0.79, 0.74, 1.47, 1.53, 1.53, 1.53
10	6.3, 6.6, 5.2
25	17.07, 17.2

Table 6.1: VIV frequency for 12 case from validation step.

order to prove it is fluid driven motion, the fluid frequency for the same run must be verified, since it was unclear at the validation step.

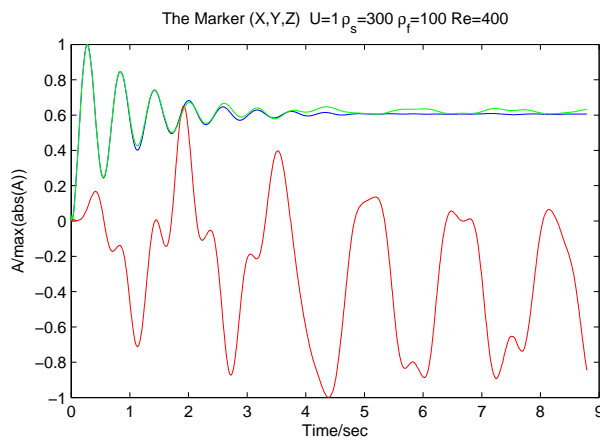


Figure 6.9: The X,Y,Z components of the marker point at $U=1 \text{ ms}^{-1}$. The lower graph is Y component.

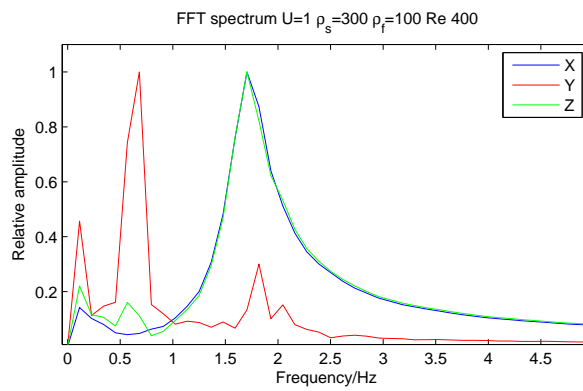


Figure 6.10: The FFT on marker point at $U=1 \text{ ms}^{-1}$. FFT on Y have maximum peak at 0.7 Hz

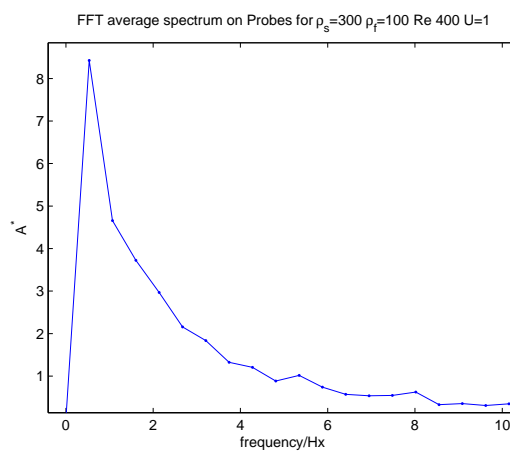


Figure 6.11: The averaged FFT spectrum for the fluid probes for $U=1 \text{ ms}^{-1}$.

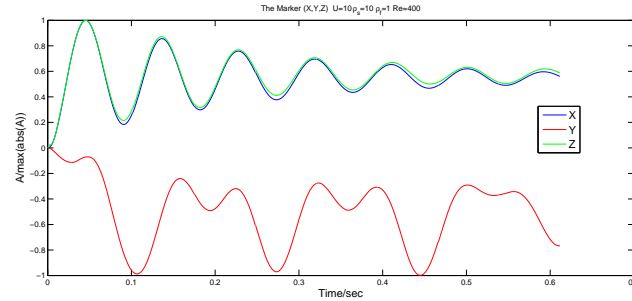


Figure 6.12: The coordinates of the marker points for $U=10 \text{ ms}^{-1}$. The lower graph is Y component

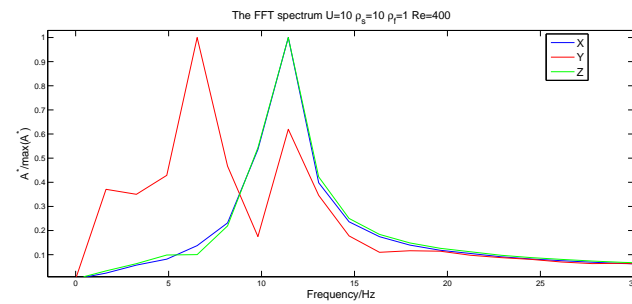


Figure 6.13: The FFT on marker point for $U=10 \text{ ms}^{-1}$. FFT on Y have two peaks, the natural frequency and fluid frequency.

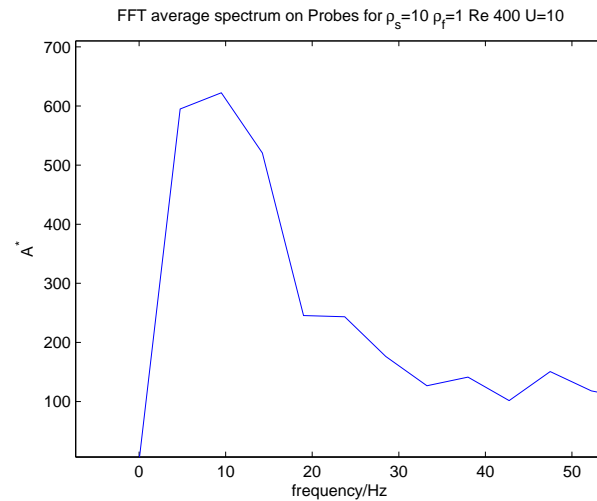


Figure 6.14: The averaged FFT spectrum of the fluid probes for $U=10 \text{ ms}^{-1}$.

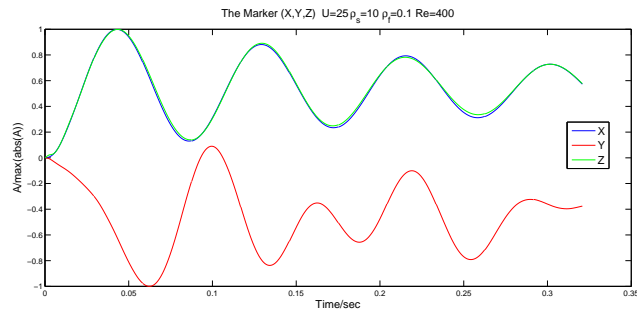


Figure 6.15: The coordinates of the marker point for $U=25 \text{ m s}^{-1}$. The lower graph is Y component

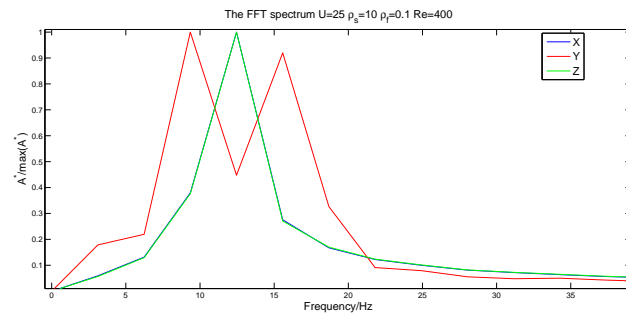


Figure 6.16: The FFT analysis of the marker point for $U=25 \text{ m s}^{-1}$. FFT on Y gives two peaks, a failed representation of the sinusoidal shape.

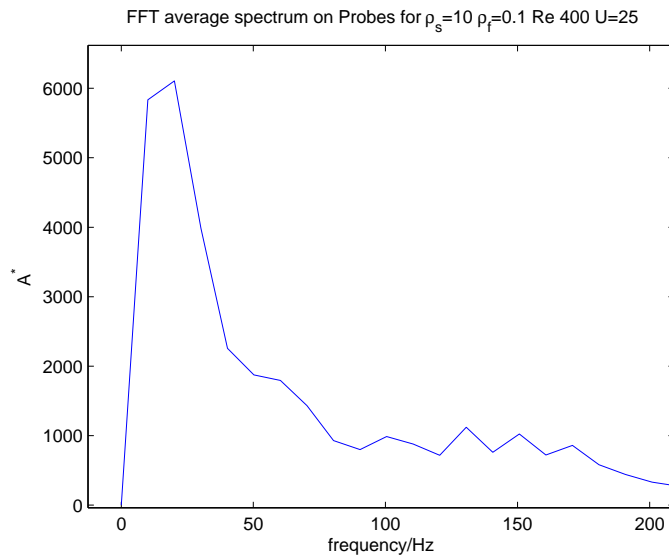


Figure 6.17: The averaged FFT spectrum for the fluid probes for $U=25 \text{ m s}^{-1}$.

Chapter 7

Discussion

This report presents a method to resolve the fluid-structure interaction (FSI) using a fixed-point iterative scheme with a partitioned Gauss-Seidel technique accelerated with Aitkens relaxation method. The observed stability of the method is limited by the inherited requirement to meet the stability in the OpenFOAM and DEAL.II, a classical feature when using a coupled solver which has different floating point error propagation. The validation of the solver involves,

- reproduced frequency shift in in-line movement to Eqn (2.62).
- matched frequency in VIV with probes of fluid and solid.
- reproduced VIV frequency with regard to Eqn (6.1).
- correlation in magnitude of amplitude with regard to Eqn (2.63).
- independence in frequency with respect to flow velocity.
- scaling in frequency cp to T_v for $\frac{\rho_f}{\rho_s} \ll 1$.

The open source packages with their libraries and tutorials, DEAL.II and OpenFOAM already contain the routines to solve the equations in question, and thus the average change in existing code files necessary to merge the packages is a minor coding effort. One of the goals was to learn to use the packages as to become tools in future projects. The actual thesis is fulfilling that goal. The essential achievement is thus the implementation and the verification of the FSI algorithm on above points. The Eqn (4.8) is of limited use, restricted to the cantilever case and the same conditions to fulfill the Bernoulli's equation. The application to the multi-cantilever case show promising feature and flexibility for a small additional cost of coding.

The application to the VIV is rather a process in verification of the success in merging the packages than an actual achievement in itself since the mesh is too coarse to have any scientific value. However, during this verification some insight of the stability of the method and model effects as boundary conditions and wall, revealed plausible future research fields which are not covered fully in the literature. In all strong VIV cases, a damping is observed, more importantly, not observed in other cases as clearly, which is more an coincidence since the damping of the same order for all cases, reducing it to the steady state level for low amplitudes ($< 1 \cdot 10^{-2}$ m), and in the region of 10^{-2} m the in-line motion is damped to the steady state level but the VIV is stronger in energy introduced by the diverted flow around the body and therefore visible clearly.

The implicit coupling and the explicit scheme in the FSI is relatively similar in convergence and stability for relative mass $\frac{\rho_f}{\rho_s} < 1$ and moderate large E , in other words, unless the pressure change by the fixed-point iteration is of comparative order as the original pressure difference due to the flow. This instability arise whenever a counter pressure induced by deformation in *one* sub-cycle iteration creates a self induced vibration which is diverging for undamped case. The convergence pattern for the Aitkens relaxation is fully reproduced as Tukovic [53] and Küttler [33] reported were to given relative mass, same level of iterations in sub-cycle was observed. The ROM method didn't improve in this region of precision, the convergence, but a significant decrease was observed in the final error in the final iteration by one to three order of magnitude than the tolerance. It is expected that the use of a better interpolation technique would improve the result.

The application itself was pressed to its limits by the Co close to 0.9, the recommended value is less than 0.5 stated in the manuals. The higher order frequencies in the marker point FFT spectrum, implicates a Crank-Nicholson error. However from the study of the isolated solid cases revealed no such bias. It's therefor believed to be a physical interaction described by the fluctuations of the vortices release at the top of the cantilever giving longitudinal waves. Some of the problematic issues in the simulations encountered can be summarized as,

- The drifting in convergence by $\gamma_i \rightarrow 0$ is caused by inadequate setting of tolerance in AutoMesh and DynamicElastic.
- Discontinuity in restart caused by the lost topological mapping between simulations. An unfortunate feature of DEAL.II.
- The coarse fluid mesh introduce large error at higher velocities and introduces the back-flow error.
- Vortex induced error in time due to zeroGradient patch.
- Mesh deformation of non-convex domain causes divergence in pressure correction.
- PISO correction extensive in FSI. One extra loop introduced to gain stability compared to no FSI.

Error analysis showed that FSI gives no additional instability and error to the flow. The error is mainly originated by the convective term and it increases linearly with the inlet velocity and some cells with possible divergence in the grid caused by the scaling from the cantilever gave points of interest where spontaneous fluctuations of velocity creates oscillations of pressure in similar fashion as the vortex-induced oscillations at the outlet but in this case they are clear in the spatial discretization.

The reader should be kindly reminded that there is no problem to find simulations that don't have the presented divergence properties while discussing numerical error in this thesis, but the error analysis combined with the limited time in the study justify the presence of these flaws in the result. This as long the error can be estimated and that the FSI algorithm does not amplify the error. On the other hand, for the purpose of validation, the actual presence is more a strength than a weakness of the result. The discretization error due to CD was exemplified showing point of spontaneous fluctuations around the corner in the course material for the project course TME050 at Chalmers [71]. These are similar to those seen in Figure 6.3 and 6.4 around the cantilever.

The failure in convergence of the Aitkens relaxation occurs whenever the correlation γ_i from Eqn (2.66) goes under a threshold and the iterative scheme is aborted. The effect of this is

then a drift of the order of the tolerance times the number of iterations from the previous converged point. By choosing the tolerance in the fluid mesh *Automesh* compared to the tolerance of convergence in Aitkens relaxation to one order magnitude less, often resolves this but not always. This since in the multi-block case it has been observed several cases of divergence in the pressure correction step. The discontinuity shift observed at the restart of simulation is due to the auxiliary class *setBoundaryIndicator*, this is directly related to the proximity distance classification using a simplified estimation of the displacement, the average, creating a shift, an off-set error. However the effect is marginal and can in most cases be corrected by post-processing the data unless the shift itself induces a change in the oscillation, observed in one case of 23 in the Y direction, one of the strong VIV cases. The convergence problem in the multi-block case is mostly related to the PISO correction and ALE deformation using elliptic integral technique, these involve a laplacian to be solved, which becomes unstable and by increasing the number of PISO loops a significant improvement is achieved (>2), or by setting the tolerance for the deformation of mesh point to an adequate level (trial and error). The extra PISO loop compared to steady flow calculation with no FSI was also necessary for the single cantilever case, and in one simulation, the pressure correction failed with divergence as a result. The exact cause to this error is unknown but as indicated in literature, when the mesh is too fine, and the change is too large, a change in the nodes which alter the topological mapping is more prominent in non-convex domains. An observed complication is the back flow at the outlet, this phenomena arise from the zero gradient boundary condition causing divergence. The largest source of error is however the limited time in simulation, forcing to high Co and rough estimates of the time periods, before transient movement enter the steady state movement.

Chapter 8

Future work

The largest source of error lies in the time required to simulate the periods to a desired accuracy to estimate the frequency, this implicates the need to use the Message Passing Interface (MPI). This allows parallel processing, a desirable and feasible feature. The current major source of model error is the mapping between the mesh and the interpolation of transfer steps. The accuracy will be improved in the transfer by changing the current transfer step to a mapping between fluid face center and solids face quadrature points. This would resolve the glitch in the restart of a job and the associated error in the evaluation of the viscous traction. This due to the artificial blown up error by using the displacement field as source of boundary field for velocity for high convective case. An impact of this is that it also allows to reduce the solid mesh size by allowing higher order elements to be used. As for example, the cantilever, by including third order elements is sufficient, allowing *one* block is to be exact, within the Bernoulli's kinematic assumption of interaction.

- implement MPI for parallel processing
- mapping between fluid face center to solid quadrature points
- change strain measure
- implement (POD) ROM
- investigate the mechanism in pressure coupling in current FSI
- implement BC for the multi-block case
- implement the buffeting effect on FSI
- implement under-integration
- adaptive meshing in fluid domain using `icoEstimateError`

This is currently impossible since then only one pressure point will be transferred, the average pressure on each side. The deviation in frequency in this project was the observed boundary condition effect on the pressure and the wall effect, this is a suitable application of the algorithm. The use of ROM to reduce the computational cost is a complicated feature since due to white noise and FD scheme implicate divergence, the work around is to use a modal analysis and expand the time steps in terms of selected eigenvectors or residual error method solved by Gauss Newton solution technique. A change in the strain measure, by going from

the small strain to the Cauchy-Green measure is important in order to raise the code from master thesis level into research level, especially since small stress tensor requires smaller deformation than 2% in order to be of scientific value. The issue with the observed twisting of the cantilever in the verification of the solid solver have its origin from the shear and volumetric locking phenomena, and hence the solution to this is using under-integration with a small effort change in creating the stiffness matrix [19].

A major improvement in the key associative mapping can be implemented by storing the distance mapping from previous run and by threshold assign the mapping function and thereby change the order for $\chi_{s \rightarrow f}$ from $O(N \cdot M)$ to $O(N)$ where N is the solid center face points and M the fluid and vice versa $O(M)$ for $\chi_{f \rightarrow s}$. The first version using quasi-static approximation failed due to improper settings in case, the question is whether this is suitable for cases with $KC \geq 5$ as proposed by [5], the code have the benefit of allowing arbitrary deformations and with a proper viscous material modelling it is assumed that modeling flexible structures as rubber materials is a feasible task. The adaptive meshing is an important task for making the FSI useful for VIV studies. The error lies in the wake and the vortices. By refining the fluid mesh using `icoErrorEstimate` has been a successful task according to OpenFOAM forum. Several reports indicates the significant gain by this procedure in accuracy to given mesh and thus allowing coarser mesh and in turn faster simulations. A question mark must be set regarding the oscillation error, whether it is a numerical or a physical consequence of an inadequate modeling of the solid. The current BC allows only natural Dirichlet condition on a stationary boundary. There is however a small task to allow the boundary to be attached to a movable boundary. Finally, allowing turbulence is an important extension in order to fully estimate buffeting, this again a smaller task, a modification in the traction vector.

A complementary literature study revealed the presence of few master thesis on the same subject, one of particular interest is the one written by Michael Stöckli [49] and PhD report with code on FeniSC, where the simplicity of the code is an appealing feature and the question arise whether future development favor this package, however, material modelling often require significant change in the inner structure of the assemblage, the question is if this can be a doable task. Further, if MPI cannot be implemented on this platform the actual beneficiary feature of DEAL.II is lessened and if also adaptive meshing was feasible in FeniSC then a change is an obvious consideration since current version contain only a non-parallelized adaptive mesh solver[73].

Bibliography

- [1] Alexander Aitken, "On Bernoulli's numerical solution of algebraic equations", *Proceedings of the Royal Society of Edinburgh* **46** (1926) 289-305.
- [2] M. Amabili, "Reduced order P.O.D Models for nonlinear vibrations of cylindrical shells with F.S.I."
<http://fluid.ippt.gov.pl/ictam04/text/sessions/docs/FSM4/12742/FSM4-12742.pdf>
- [3] K.J. Bathe, H. Zhang and M.H. Wang, "Finite Element Analysis of incompressible and compressible fluid flows with free surfaces and structural interactions." *Computers and Structures* **56**(2-3) (1995) 193-213 .
- [4] Klaus-Jürgen Bathe and Hou Zhang, Shanhong Ji, "Finite element analysis of flows fully coupled with structural interactions", *Computers and Structures* **72** (1999) 1-16.
- [5] P.W. Bearman, J.M.R. Graham and E.D. Obasaju, "A model for transverse forces on cylinders in oscillatory flows." *Applied Ocean Research*, **6**(3) (1984) 166-172.
- [6] Peter Bearman and Mäsa Brankovic, "Experimental studies of passive control of vortex-induced vibrations." *European Journal of Mechanics B/Fluids* (2004) 9-15.
- [7] K. Yusuf Billah and Robert H. Scanlan, "Resonance, Tacoma Narrow bridge failure and undergraduate physics textbooks." *Am. J. Phys.* **59**(2) (1991) 118-124 .
- [8] Frederic J. Blom, "A monolithic fluid-structure-interaction algorithm applied to the piston problem." *J. Comput. Methods Appl. Mech. Engrg* **167** (1998) 369-391.
- [9] C.L. Cunff, F. Biolley, E. Fontaine, S. Étienne and M.L. Facchinetti, "Vortex-Induced Vibrations of Risers. Theoretical, Numerical and Experimental Investigation", *Oil, Gas and Tech, Rev, IFP.* **57**(1) (2002) 59-69 .
- [10] P.D'asdia and S.No, "Vortex-Induced Vibration of reinforced concrete chimney: in situ experimental and numerical prevision." *J. Wind Engineering and Industrial Aerodynamics* **74-76** (1998) 765-776.
- [11] J. Donea Antonio Hueste, J.Ph. Ponthot and A. Rodriguez Ferran, *Arbitrary Lagrangian-Eulerian Methods, Encyclopedia of Computational Mechanics*, volume 1 chapter 14. (2004) John Wiley & Sons.
- [12] Einstein, Albert, "The Foundations of the General Theory of Relativity", *Annalen der Physik* **6**(30) (1916) p.74
- [13] Earl H. Dowell and Kenneth C Hall, "Modelling of fluid-structure interaction." *Ann. Rev Fluid. Mech.* **33** (2001) 445-90.

- [14] Edda Eich-Soellner and Claus Führer, *Numerical Methods in MultiBody Dynamics*. Teubner-Verlag Stuttgart. Course book for FMN110, my assignement is with own data by similar context is found in this book.
- [15] C.Farhat and M.Lesoinne, "Two efficient staggered algoritm for the serial and parallel solution of three-dimensional nonlinear transient aeroelastic problems." *Comput. Meth. Applied Mech. Engrg.* **182** (2000) 499-515.
- [16] Zhengkun FENG and Azzeione Soulaïmani, "Nonlinear aeroelastic modeling using a reduced order model based on proper orthogonal decomposition", Proceedings of Proceedings of PVP2007. ASME. *Pressure Vessel and Piping Division*. July 20-26, 2007. PVP2007-26006.
- [17] J. H. Ferziger, M. Peric, *Computational Methods for Fluid Dynamics*, Springer, 3rd Ed., (2001).
- [18] F.Flemming and C.H.K. Williamson, "Vortex-induced vibrations of a pivoted cylinder." *J. Fluid. Mech.* **522** (2005) 215-252.
- [19] Magnus Fredriksson, Doctoral Thesis, *Class of accurate low order finite elements*. Division of Solid Mechanics LTH (2006).
- [20] A.L.C. Fajarra, C.Pesce, F.Flemming and C.H.K.Williamson, "Vortex-induced vibration of a flexbible cantilever." *J. Fluids and Structures* **15** (2001) 651-658.
- [21] R.D.Gabbai and H. Benaroya, "An overview of modeling and experiments of Vortex-Induced Vibrations of Circular Cylinders." *Journal of Sounds and Vibration* **282** (2005) 575-616.
- [22] Jean-Frédéric Gerbeau , Marina Vidrascu , "A Quasi-Newton Algorithm Based on a Reduced Model for Fluid-Structure Interaction Problems in Blood Flows." *ESAIM: Mathematical Modeling and Numerical analysis*, **137**(4) (2003) 631-647.
- [23] M.Geradin and D.Rixen, *Mechanical vibrations, Theory and Application to Structural Dynamics* (1997) Second Edition WileyBlackwell.
- [24] Daniel Green and William G.Unruh, "The failure of the Tacoma Bridge: A physical model." *Am. J. Phys.* **74** (8) 706-716 (2006).
- [25] Daisuke Ishiara and Shinbou Yoshimura, "A monolithic approach for the interaction of incompressible viscous fluid and an elastic body based on fluid pressure Poisson equation." *Int. J. Numer. Meth. Engng.* **64** (2005) 167-203.
- [26] Laural Jacquin, "Aircraft trailing vortice: An introduction." *C.R.Physique* **6** (2005) 395-398.
- [27] H.Jasak and H.G. Weller, "Application of the finitie volume method and unstructured meshes to linear elasticity." *Int. J. Numer. Meth. Engng.* **48** (2000) 267-287.
- [28] Hvroje Jasak, Doctoral Thesis, *Error Analysis and Estimation for the finite Volume Method with Application to Fluid Flows*, Imperial college, University of London, 1996.
- [29] Cristophe Kassiotis, "Which strategy to move the mesh in the computational fluid dynamic code in OpenFOAM"
<http://powerlab.fsb.hr/ped/kturbo/OpenFOAM/slides/>.

- [30] D.W. Kelly, J.P. Gago, O.C. Zienkiewicz, I. Babuska, "A posteriori error analysis and adaptive procedure for practical engineering analysis", *Int. J. Numer. Methods Eng.* **19** (1983) 1593-1619.
- [31] T.Kitagawa, Y.Fujino and K.Kimura, "Effects of free-end condition on end-cell-induced vibration." *J. Fluid and Structures* **13** (1999) 499-518.
- [32] Raghavan A. Kumar, Chan-Hyun Sohn and Banglaore HL.Gowda, "Passive control of Vortex-induced vibrations: An overview." *Recent Patents on Mechanical Engineering* **1** (2008) 1-11.
- [33] Ulrich Küttler, Wolfgang A. Wall. "Fixed-point fluid-structure interaction solvers with dynamic relaxation". *Comput.Mech.* **43**(1) (2008) 61-72.
- [34] Fabian Peng Kärrholm, "Rhie-Chow interpolation in OpenFOAM", Appendix from *Numerical Modelling of Diesel Spray Injection and Turbulence Interaction* at Chalmers University.
http://www.tfd.chalmers.se/hani/kurser/OS_CFD_2007/rhiechow.pdf
- [35] Lieve Lanoye, "Challenges in realizing vascular fluid-structure-interaction using Fluent and Abaqus software."
http://sympos.elis.ugent.be/archive/symp2006/papers_poster/paper037_Lieve_Lanoye.pdf
- [36] Anders Logg, "Automating Finite element method." *Arch. Comput. Methods Eng.* **14** (2006) 93-138.
- [37] Hermann G.Matthies and J.Sterndorf, "Partitioned strong fluid coupling algorithms for fluid-structure interaction." *Computers and Structures* **81** (2003) 805-812.
- [38] Sanjay Mittal and Sauray Singh, "Vortex-induced vibrations at subcritical Re." *J. Fluid.Mech.* **534** (2005) 185-194.
- [39] Prioiz Moradnia, Phd course report on IcoDymFoam,
http://www.tfd.chalmers.se/hani/kurser/OS_CFD_2007/PiroozMoradnia/OpenFOAM-rapport.pdf
- [40] Tikeswar Naik , Ellen K. Longmire, S.C. Mantell , "Dynamic response of a cantilever in liquid near a solid wall." *Sensor and Actuators A* **102** (2003) 240-254.
- [41] J.M.T. Penrose,D.R. Hose, C.J. Staples, I.S. Hamill, I.P. Jones and D. Sweeney," Fluid-structure interactions: coupling of CFD and FE." *CAD-FEM User Meeting Internationale FEM-Technologietage*. Sept 2001.
- [42] Prandtl and Tietjens, Applied Hydro and Aeromechanics, Figure 60, Dover, ISBN 0-486-60375-X.
- [43] M.Razzaq, Jhron and S.Turek, "Numerical simulation of laminar incompressible fluid-structure interaction for elastic material with point constraints." PDF draft document from Institute of Applied Mathematics, TU Dortmund, Germany, submitted for publication and accepted, Springer, Berlin (2008).
- [44] Vincent Rivola, "Comparative Study of the CFD codes Mistral and OpenFOAM - Application to fluid-structure interaction."
<http://powerlab.fsb.hr/ped/kturbo/OpenFOAM/slides/>

- [45] Takaaki Sakai Koji Iwate, Masaki Morishita and Seiji Kitamura, "Vortex-Induced Vibrations of a cantilever circular cylinder in super critical Reynolds Number Flow and its suppression by Structure Damping." *JSME Series B* **44**(4) (2001) 712-720.
- [46] Göran Sandberg, *CALFEM: Acoustic and interface elements for structure-acoustic analysis.* (2001) Structural Mechanics LTH, Sweden.
- [47] Marianne Shubov, "Mathematical modeling and analysis of flutter in long-span suspended bridges and in blood vessel walls", *J. Aerospace Engineering* **17**(2) (2004) p. 70
- [48] Marianne Shubov, "Mathematical modeling and analysis of flutter in bending-torsion, coupling beam, rotating blades and hard disk drives", *J. Aerospace Engineering* **17**(2) (2004) p. 56
- [49] Michael Stöckli, *A Unified Continuum Fluid-Structure Interaction Solver using an ALE finite Element Method. An Investigation on how to simulate blood flow.* Master of Science Thesis, KTH, Stockholm, Sweden 2007.
- [50] P.A.B. de Sampaio P.H.Hallak, Alvaro. L.G.A Coutinho and Michéle S. Pfeil , "A stabilized finite element procedure for turbulent fluid-structure interaction using adaptive time-space refinement." *Int. J. Num. Mech. Fluids*, **44** (2004) 673-693.
- [51] Robert H.Scanlan, "An observation on Low-Speed Aeroelasticity", Amer. Soc. 150th Anniversary Civilengineer paper, Conference paper. <http://cedb.asce.org/cgi>, by Jeffrey S. Russell, (editor) Reston, VA: ASCE, 0-7844-0686-3, (2003), p. 401.
- [52] C.Trusedell and K.R. Rajagopal, *An Introduction to the Mechanics of Fluids*, Birkhäuser.
- [53] Zeljko Tukovic Hrvoje Jasak, "Updated Lagrangian finite volume solver for large deformation response of elastic body." *Transaction of Famena* **30**(2) (2007) 1-18
- [54] Jan Vierendeels, "Implicit Coupling of partitioned fluid-structure interaction solvers using reduced order models". *Comp. and Struct.* **85**, Issue 11-14, (2007) 970-976
- [55] Stefan Wagert, Markus Dreier and Martin Hegner, "Frequency shifts of cantilevers vibrating in different various media." *Appl. Phys. Letter.* **69** (19), Nov 4. (1996) 2834-2836.
- [56] H.G. Weller, G. Tabor, H.Jasak and C.Fureby, "A tensorial approach to computational continuum mechanics using object-oriented techniques." *Computers in Physics* **12** No. 6 Nov/dec (1998) p. 620 .
- [57] C.H.K Williamson, "Advances in our understand of vortex dynamics in bluff body wakes". *J. Wind Engineering and Industrial Aerodynamics* **69-71** (1997) 3-32.
- [58] C.H.K. Williamson and R. Govardhan, "Vortex-induced vibrations". *Ann. Rev.Fluid.Mech* **36** (2004) 443-455.
- [59] Li Zhou and Yajun Ge, "Wind Tunnel Test for Vortex-Induced Vibration of Vehicle-Bridge system section model", *J. Braz. Soc. Mech. Sci. and Eng.* **30**(2) (2008) 110-117.
- [60] OC Zienkiewicz, RL Taylor, JZ Zhu *The Finite Element Method: Its Basis and Fundamentals*,(2005). Elsevier Ltd.
- [61] The homepage <http://www.dealii.org>. A collection of papers in how using deal.II at <http://www.dealii.org/developer/reports/>.
- [62] <http://www.comsol.com/products/multiphysics/>.
- [63] <http://www.fluent.com/solutions/aerospace/pdfs/nl559.pdf>.
- [64] <http://www.ansys.com/solutions/fsi.asp>.

- [65] OpenCFD Ltd produce *OpenFOAMTM*, the open source computational fluid dynamics (CFD) toolbox <http://www.opencfd.co.uk/openfoam/>, Recommended sublink for a collection of papers and slides on the subject, <http://powerlab.fsb.hr/ped/kturbo/OpenFOAM/slides/>.
- [66] <http://femcodes.nscee.edu/src/Benchmark.pdf>.
- [67] <http://www.lstc.com/>.
- [68] <http://en.wikipedia.org/wiki/>, on search karman vortex street. Note however that is several different formulas for different Re they are however closely related and difference lies in what source used and experiments performed.
- [69] http://www.cs.rpi.edu/~szymansk/OOF90/F90_Objects.html.
- [70] http://www.amath.washington.edu/~lf/software/CompCPP_F90SciOOP.html.
- [71] http://www.tfd.chalmers.se/~hani/kurser/OS_CFD_2008/.
- [72] http://en.wikipedia.org/wiki/Fluid-structure_interaction.
- [73] <http://fenics.org>.
- [74] <http://www.python.org>.
- [75] <http://caelinux.com>.

[All links are update to the present date of presentation of the thesis.]